1 km annual forest cover and plant functional types dataset for China from ~~1980~~ 1981 to 2023

Bo Liu [1], Boyan Li [1], Fulai Feng [1], Yangcan Bao [1], Jing Li [1], Qi Feng [1,2]

[1]School of Geography and Tourism, Shaanxi Normal University, Xi'an, 710119, PR China
[2]Key Laboratory of Ecohydrology of Inland River Basin/Gansu Qilian Mountains Eco-Environment Research Center, Northwest Institute of Eco-Environment and Resources, Chinese Academy of Sciences, Lanzhou, 730000, PR China

Correspondence to: Boyan Li (byli@snnu.edu.cn) Qi Feng (qifeng@lzb.ac.cn)

Abstract. High-~~-~~spatial-~~-~~resolution and long-term data on forest cover and plant functional types (PFTs) are crucial for elucidating the impacts of forest cover change on the national terrestrial carbon balance. Since the 1980s, China has undergone a substantial expansion in its forest area, primarily driven by large-scale national afforestation programmes. However, existing land cover products have often failed to capture this long-term increasing trend, leading to an underestimation of forest cover change–related ecological processes. Here, we developed a high-resolution (approximately 1 km), annual forest cover dataset for China during ~~1980~~1981–2023. This dataset integrates spatial constraints from multi-source remote sensing data with provincial-level statistics from China's national forest inventories (NFIs), providing a consistent and spatially explicit record of forest dynamics over four decades. Building on this primary dataset, we further produced an annual PFT dataset that disaggregates total forest cover into ~~eight~~ nine distinct plant functional types, suitable for use in dynamic global vegetation models (DGVMs). Validation against independent data indicates that our reconstructed dataset achieves an overall accuracy (OA) of 84.86% ± 1.18% for five aggregated forest types (evergreen needleleaf forests, evergreen broadleaf forests, deciduous needleleaf forests, deciduous broadleaf forests, and mixed leaf forests), and it reproduces NFI-consistent forest dynamics ($R^2 \approx 1$). ~~Validation against independent data confirms the dataset's ability to accurately represent historical forest recovery, achieving an overall accuracy (OA) of 95.3 ± 0.5%, with classification accuracies for needleleaf and broadleaf forests ranging from 84.4% to 92.0%.~~ To evaluate its applicability, we implemented the dataset within the Lund–Potsdam–Jena General Ecosystem Simulator (LPJ–GUESS). Compared to the widely used PFT dataset from the European Space Agency's Land Cover Climate Change Initiative (ESA CCI) and the MODIS land cover type product (MCD12Q1), our product yields a markedly improved simulation of key biophysical and biogeochemical processes in China, reducing the simulation errors for evapotranspiration, leaf area index (LAI), and vegetation carbon flux across 63.1%–85.3% of China's terrestrial area~~enhancing the accuracy of evapotranspiration, leaf area index (LAI), and vegetation carbon flux by 49.4%–77%~~. With its high spatial resolution, long-~~-~~term temporal coverage, and detailed forest-type classification, our dataset offers a robust foundation for assessing the ecological impacts of forest restoration and for constraining estimates of China's forest carbon sink since ~~1980~~1981. The dataset is freely available at 10.5281/zenodo.17656153~~10.5281/zenodo.16208012~~ (Liu et al., 2025).

1 Introduction

Large-scale afforestation programmes were implemented in China during the past four decades (Tong et al., 2018; Chen et al., 2019). As a result, forest area in China increased to around 230 million hectares, a rise of 100% compared to the early 1980s (IDS, 2018). Recent satellite observations revealed widespread "vegetation greening patterns" in China due to several large-scale conservation programmes (Piao et al., 2020). These changes have significant implications for carbon dynamics and ecosystem services. Specifically, they have enhanced carbon sequestration, reduced soil erosion and acidification in northern China, and altered regional climate patterns through changes in surface albedo, evapotranspiration, and aerodynamic roughness (Liu et al., 2017; Hong et al., 2020). These findings underscore the critical role of afforestation in mitigating climate change and improving ecosystem stability at regional and global scales (Alkama and Cescatti, 2016; Yang et al., 2024).

Despite these positive developments, precisely quantifying the contribution of these land cover changes to the global carbon balance remains a significant challenge (Li et al., 2025; Yu et al., 2024). During the period 2014–2023, the net carbon emissions from the global land use, land use change, and forestry (LULUCF) sector were estimated at 4.1±2.6 Gt CO_2 yr^{-1}, accounting for 10% of total anthropogenic CO_2 emissions (Friedlingstein et al., 2024). The uncertainty of this estimate exceeds 50% of the mean flux, making LULUCF the most uncertain component in the global carbon budget (Friedlingstein et al., 2024; O'Ssullivan et al., 2022). These uncertainties primarily arise from disparities in model process representation, inconsistencies in flux definitions, variability in management practices, and spatiotemporal estimation differences in forest cover and its change rates (Ruehr et al., 2023; Hartung et al., 2021; Yu et al., 2022).

Although remote sensing has greatly improved the availability of land use and land cover ~~change~~ (LULCC) data, discrepancies among different datasets regarding the estimation of China's forest area propagate large uncertainties into modelling (Tu et al., 2024; Zhu et al., 2025); for instance, it has led to three- to five-fold differences in estimates of China's terrestrial carbon storage from similar bookkeeping models (e.g., 17–33 Pg C vs~~.~~ 6.18 Pg C from 1700 to 2000) (Houghton and Hackler, 2003; Ge et al., 2008). Cross-dataset comparisons highlight the scale of this issue: estimates of China's forest area for the year 2010 from five different forest datasets ranged from 1.74 to 2.27 million km^2, a relative difference of 29% (Qin et al., 2015). Peng et al. (2024b) compared eight LULC datasets for the year 2020 and found a maximum discrepancy of 0.34 million km^2, an amount equivalent to 15% of the area reported by the national forest inventory (NFI). This inter-product inconsistency is notable, as it appears inconsistent with the widely reported trend of forest expansion in China. According to NFI data, the nation's forest area more than doubled from 1.15 million km^2 in 1981 to 2.31 million km^2 by 2021 (IDS, 2018). This trend is consistent with broader assessments by the Food and Agriculture Organization of the United Nations (FAO), which attribute the shift in Asia's forest balance from a net loss in 1990–2000 to a marked net gain in 2000–2010 primarily to China's sustained afforestation efforts (FAO, 2016). However, long-term satellite-based LULC products often fail to capture this marked increase (Yang and Huang, 2021). For example, the GlobeLand30 product shows a relatively small expansion of 5,700 km^2 between 2000 and 2020 (Chen et al., 2015), while the national land cover database of China (NLCD–China) indicates a net loss of 14,000 km^2 from 2001 to 2015 (Wei et al., 2024). Consequently, due to these disagreements among

datasets, the contribution of the LULUCF sector to China's regional carbon budget is subject to uncertainty~~remains poorly constrained~~ (Xia et al., 2023; Yu et al., 2022).

The NFI is considered the foundational national dataset for quantifying forest cover and biomass stocks (Zeng et al., 2015; Xia et al., 2023). Since the implementation of the second NFI during 1977–1981, a standardized sampling and survey methodology has been applied nationwide. Subsequently, eight further NFI campaigns have been conducted on a continuous five-year cycle (IDS, 2018). Owing to its extensive sample size covering the entire country, the forest area statistics provided by the NFI are widely regarded as a reference dataset. This large-scale inventory provides unique bottom-up information that complements top-down data from satellite remote sensing products, ensuring that the spatiotemporal dynamics of land use activities are accurately captured. Indeed, previous studies have ~~utilized~~utilised the NFI dataset to estimate the national forest carbon budget (Fang et al., 2001; Piao et al., 2009). However, a key limitation of the NFI is that it only publicly provides forest area statistics at the coarse provincial level. This spatial aggregation constrains its direct application for simulating carbon dynamics in spatially explicit E~~e~~arth system models (Zhu et al., 2025).

At both global and national scales, dynamic global vegetation models (DGVMs) typically represent key vegetation processes—such as photosynthesis and evapotranspiration—using a simplified classification of globally representative plant functional types (PFTs) that exhibit similar ecological and physiological traits (Gregor et al., 2024; Bergkvist et al., 2025), and they are typically defined by traits including photosynthetic pathway (C3/C4), leaf morphology (needleleaf/broadleaf), and phenology (evergreen/deciduous) (Islam et al., 2024). Research has shown that explicitly incorporating forest restoration processes into DGVMs is critical not only for quantifying their feedback on the carbon cycle, surface energy balance, and the climate system, but also for providing a science-based foundation for policy assessment (Yue et al., 2024; Peng et al., 2024a). To accurately simulate carbon dynamics and vegetation succession, this requires the models to be driven by annually updated PFT distribution data (Pugh et al., 2024). However, a high-resolution, annual ~~time series~~time series dataset that accurately reflects the PFT composition and spatial distribution during China's recent forest restoration is currently lacking (Yu et al., 2022; Xia et al., 2023). Most existing forest cover products either provide only single-year classifications or offer PFT information at coarse temporal resolutions, failing to meet the annual input requirements of DGVMs (Ran et al., 2012). Furthermore, they often fail to capture the forest recovery trends documented by NFI. While some recent studies have developed NFI-based reconstructed forest datasets, these products are typically either too coarse in spatial resolution (e.g., 0.5°), do not provide the distribution of individual PFTs, or are not temporally continuous, with maps produced only every ~~several~~ few years (Yu et al., 2022; Xia et al., 2023). Therefore, there is an urgent need to generate NFI-consistent, high-resolution, and annually resolved long-term maps of both forest cover and PFT distribution. Such a dataset is fundamental for robustly assessing China's forest carbon sink and its driving factors using ecosystem models.

In this study, we developed a novel method that fuses the temporal constraints from statistical inventories with the spatial constraints from remote sensing data to identify the distribution of forest PFTs. We integrated provincial-level forest area statistics from the NFI for ~~1976~~1981 ~~–2021~~ 2023 with nearly all available LULC and auxiliary remote sensing products. This allowed us to first reconstruct annual changes in China's total forest cover at a 1 km spatial resolution from ~~1980~~ 1981 to 2023.

Building on this foundation, we then derived the annual distribution of ~~eight~~ nine distinct PFTs for the period 1981–~~2013~~ 2023 through a series of systematic steps, including the classification of life forms and the derivation of phenological characteristics. The overall goal of this work is twofold: first, to provide a dataset that accurately captures the spatiotemporal distribution and trends of China's forests and PFTs since the onset of its national restoration programme~~r~~s in the 1980s; and second, to demonstrate the effectiveness of this new dataset in a DGVM. To achieve this, we applied our product in the Lund–Potsdam–Jena General Ecosystem Simulator (LPJ–~~–~~GUESS) model (Lindeskog et al., 2021) and benchmarked its performance against the global PFT dataset from the European Space Agency's Climate Change Initiative (ESA CCI) (Harper et al., 2023) and the MODIS land cover type product (MCD12Q1) (Sulla-Menashe et al., 2019) in simulating key land surface variables, namely gross primary production (GPP), net ecosystem exchange (NEE), leaf area index (LAI), and actual evapotranspiration (ET)~~(GPP, NEE, LAI, and ET)~~. We present the following: (1) changes in China's forest cover and PFTs ~~in China~~ since the 1980s; (2) the historical dynamics of forest gain and loss, including their area, onset year, and duration; and (3) the performance of our reconstructed PFT distribution compared to existing global datasets when used in a DGVM. Ultimately, our dataset is expected to provide critical data support for the accurate simulation of China's forest carbon sink and the scientific assessment of its driving factors since the beginning of the nation's large-scale forest restoration.

2 Data

The forest cover and PFTs were derived from the integration of NFI data with multi-source remote sensing LULC time series data (Table 1, Table S1). The LULC data provides the spatial distribution of forest cover across different years. For specific years, the land cover classification also defined the extent of forest PFTs, based on distinctions in phenology and leaf morphology. The NFI data constrained the forest area and structural composition; this ensured that the resulting dataset aligned with reported national trends in forest area dynamics.

Auxiliary data products, such as the satellite-based normali~~s~~z~~~~ed difference vegetation index (NDVI) data (see Sect. 2.3), were used to identify potential residual forest pixels in cases of discrepancy between the LULC data and NFI data. For example, where the forest cover extracted from the LULC data was less than the area specified by the NFI for a given region, NDVI was used as a sensitive indicator of vegetation vigour. Pixels considered more likely to represent forest cover were then selected to supplement the forest area and its spatial distribution.

Table 1. Summary of datasets used in this study.

Data ~~Variable~~variable	Data ~~Type~~type	Resolution	Time range	Data ~~Source~~source
National forest inventories (NFI)	Tabular Statistics	Provincial	~~1976~~1981–~~2021~~2023	National Forestry and Grassland Science Data Center (https://www.forestdata.cn/)
Multi-source land use and land cover (LULC) products	Raster	Various, resampled to 1 km	~~1980~~1981–2023	See Table S1
~~Jeong's NDVI~~	~~Raster~~	~~0.05°~~	~~1982–2021~~	~~Jeong et al. (2024)~~

Landsat-derived normalised difference vegetation index (NDVI)	Raster	30 m	1985–2023	(Cai et al., 2025)
Climate zones	Raster	~1 km (0.0083°)	1980–2016	(Beck et al., 2018)
Topographic	Raster	1 km	Static	Amatulli et al. (2018)
1 km monthly mean temperature dataset for China	NetCDF	1 km	1981–2023	National Tibetan Plateau Data Center (https://doi.org/10.11888/Meteoro.tpdc.270961)
~~ERA5-Land~~	~~Raster~~	~~0.1°~~	~~1980–2023~~	~~Copernicus Climate Data Store (https://cds.climate.copernicus.eu/)~~

2.1 National Forest Inventories

To assess the quantity, structure, function, and productivity of its forest resources, the National Forestry and Grassland Administration of China conducted ten national forest resource inventories between 1973 and 2023. The inventories took place during the periods 1973–1976, 1977–1981, 1984–1988, 1989–1993, 1994–1998, 1999–2003, 2004–2008, 2009–2013, 2014–2018, and 2019–2023. The data are available from the National Forestry and Grassland Science Data Center (NFGSDC) at https://www.forestdata.cn/ (last access: 20 June 2025). The surveys were performed at the provincial level, employing a systematic sampling design with fixed plots located at the intersections of the national 1:50,000 or 1:100,000 topographic map grids. For each plot, recorded variables included forest cover, forest type area, and standing volume~~. This study utilized provincial-level forest area statistics from the first to the tenth NFI reports. These statistics comprise data for needleleaf forests, broadleaf forests, bamboo forests, and economically important timber forests.~~ This study utilised provincial-level area statistics from the NFI reports, specifically: area data for wooded land, needleleaf and broadleaf forests from the second through eighth inventories; arbor forest area from the ninth inventory; and total forest area from the sixth through tenth inventories.

2.2 Land use and land cover datasets

This study ~~utilized~~utilised twenty-two~~nineteen~~ datasets covering the period ~~1980~~1981–2023 as the foundational inputs for the forest cover reconstruction (Table S1). Forest cover information was extracted from these LULC products. Pre-processing of the data involved several steps: (i) reprojecting all datasets to the WGS_1984_Albers spatial reference system; (ii) resampling to a 1 km resolution using the majority~~nearest neighbor~~ method; and (iii) aligning all data to a common grid framework to ensure a consistent cell size and spatial extent for China.

2.3 Satellite-based vegetation index dataset

~~This study utilized the global long-term NDVI dataset developed by Jeong et al. (2024), which was produced by fusing data from AVHRR and MODIS. The dataset is publicly available at: https://www.environment.snu.ac.kr/data/longterm-vi (last access: 13 April 2025). The product addresses temporal inconsistencies between sensors via cross-calibration of the AVHRR~~

~~instruments, correction for orbital drift, and the fusion of AVHRR and MODIS data using machine learning techniques. It possesses a spatial resolution of 0.05° and a monthly temporal resolution, covering the period 1982–2021. In this study, the maximum growing season NDVI value served as the primary indicator for classifying "potential forest pixels" of a given consistency level as forest (see Sect. 3.2). To extend the analysis period to 1980–2023 whilst maintaining continuity, the time series was gap-filled at its ends: records for 1980–1981 were substituted with data from 1982, and records for 2022–2023 were substituted with data from 2021.~~

This study utilised China's first seamless annual leaf-on (growing season) Landsat composite dataset (1985–2023) from Cai et al. (2025). This dataset harmonises multi-sensor Landsat imagery through a comprehensive compositing method, addressing critical issues such as cloud/shadow contamination, reflectance consistency, and data gaps, thereby providing a single annual growing-season composite imagery. The dataset is available on the Google Earth Engine (GEE) platform (https://ee-caiyt33-catcd.projects.earthengine.app/view/landsat-yearly-composite-viewer, last access: 20 October 2025).

From this dataset, we derived annual growing-season NDVI data using the near-infrared (NIR) and red bands, calculated as: $(NIR - Red)/(NIR + Red)$. This data was then resampled to a 1 km resolution using mean aggregation. In this study, the growing-season NDVI served as the primary indicator for classifying "potential forest pixels" as forest (see Sect. 3.3). Owing to the scarcity of Landsat imagery in the early 1980s (Yang and Huang, 2021), and to ensure temporal consistency across the extended 1981–2023 analysis period, records for 1981–1984 were gap-filled using data from 1985.

2.4 Zonation products

To assign phenological types to the small number of remaining unclassified forest pixels (see Sect. 3.~~3~~4.2), two supplementary regional partitioning products were ~~utilized~~utilised. The first was the Köppen–Geiger climate classification from Beck et al. (2018), which classifies Earth's land surface into 30 distinct climate zones at a 0.0083° resolution (approx. 1 km) based on temperature and precipitation records from 1980–2016. The data are publicly available from Figshare at: https://figshare.com/articles/dataset/Present_and_future_K_ppen-Geiger_climate_classification_maps_at_1-km_resolution/6396959/2 (last access: 26 May 2025). The second product was a global topographic dataset from Amatulli et al. (2018), derived from the 250 m GMTED2010 and 90 m SRTM4.1dev digital elevation models. This dataset classifies the global land surface into ten topographic categories: flat, peak, ridge, shoulder, spur, slope, hollow, footslope, valley, and pit. The data are publicly available from Earthenv at: https://www.earthenv.org/topography (last access: 25 May 2025). Generally, needleleaf forests are predominantly evergreen, with the notable exception of larch forests, which are deciduous and found mainly in boreal regions. In contrast, broadleaf forests are typically deciduous, although those in tropical regions are predominantly evergreen. To further classify evergreen and deciduous forest types as either boreal/temperate or tropical (see Sect. 3.~~3~~4.3), ~~this study also utilized 2 m temperature data from the ERA5–Land reanalysis dataset. This dataset provides monthly mean climate variables at a 0.1° spatial resolution, covering the temporal range 1980–2023. The data are publicly available from the Copernicus Climate Data Store at: https://cds.climate.copernicus.eu/datasets/reanalysis-era5-land-monthly-means?tab=overview (last access: 21 September 2024).~~ this study also utilised the 1 km resolution monthly mean temperature

dataset for China (1981–2023) from Peng et al. (2019a). This dataset was generated by spatially downscaling the global 0.5° CRU climate dataset and the high-resolution WorldClim dataset using the Delta spatial downscaling method. The data are publicly available from the National Tibetan Plateau Data Center (https://doi.org/10.11888/Meteoro.tpdc.270961, last access: 27 October 2025).

3 Method

The framework for mapping forest cover and PFTs is shown ~~in~~on Fig. 1. It includes the interpolation of NFI statistical data, reconstruction of annual PFTs, validation, and modelling assessment. We constructed annual forest cover maps of China for the period ~~1980~~1981–2023 by integrating multiple data sources and derived PFTs through a sequential, multi-step process: first, classifying forest life forms~~forest life forms were classified~~ using a method analogous to the forest cover reconstruction, second, deriving phenological characteristics, and finally, subdividing these intermediate classifications into the final PFTs based on a set of climatic rules. ~~Notably, the availability of NFI data for needleleaf and broadleaf forests is restricted to the period 1981–2013. Consequently, the corresponding annual PFT maps were reconstructed only for these years.~~ Finally, the accuracy of the reconstructed dataset was assessed using validation samples from field surveys and independent reference data, and its consistency was analys~~z~~ed against existing LULC datasets. In particular, the reconstructed PFT dataset was used to drive a DGVM to evaluate the performance of the updated PFTs in simulating a series of surface fluxes by comparing them against those from a simulation using the global PFT dataset from the ESA CCI (Harper et al., 2023) and the MCD12Q1 (Sulla-Menashe et al., 2019).

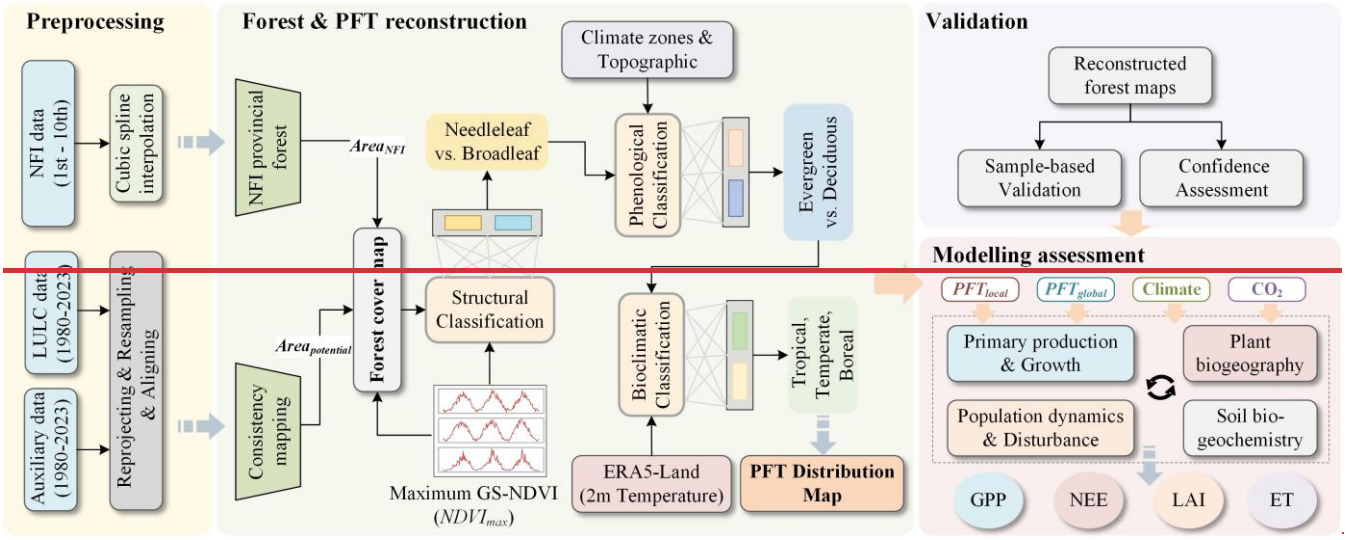

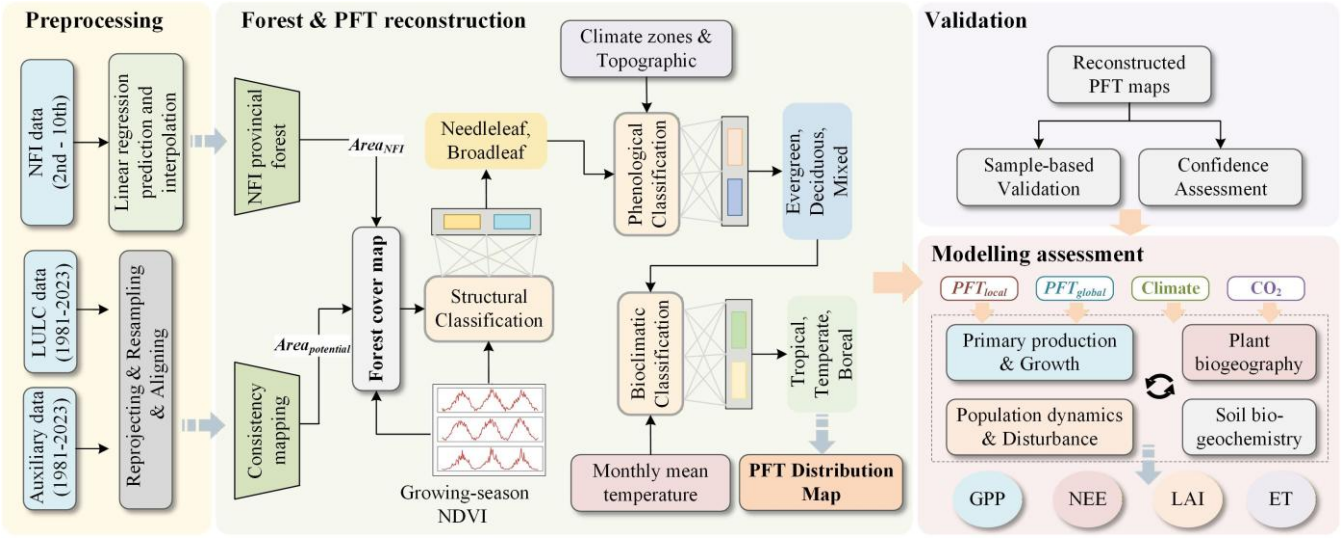

Figure 1. Flowchart for generating annual forest cover and plant functional types (PFT) maps.

3.1 Definition of forest

A clear definition of forest composition is required prior to reconstructing the PFT distribution. According to China's "Technical regulations for continuous forest inventory" (GB/T 38590-2020), China's forests are divided into categories such as wooded land, arbor forest, shrubland, bamboo forest, and economic forest, follow a specific hierarchical classification system (Table S2). The area relationships among these components are defined as follows:

$$A_{Forest} = A_{Woodedland} + A_{Shurbland} \quad (1)$$

$$A_{Woodland} = A_{Arbor} + A_{Bamboo} + A_{Econ} \quad (2)$$

$$A_{Arbor} = A_{Needleleaf} + A_{Broadleaf} \quad (3)$$

Our reconstruction method adheres to two primary constraints: (1) Forest area constraint: To ensure consistency between statistics and remote sensing data, our "forest" class is constrained using the provincial-level area of wooded land. We explicitly exclude the shrubland category. This approach aligns our statistical constraint with the "forest" class (i.e., tree-covered areas) typically identified in LULC products, excluding the "shrub" category present in some LULC products. (2) PFT area constraint: The sub-classification of PFTs is constrained using the provincial area of arbor forest, which comprises the needleleaf and broadleaf categories (Table S2). Notably, the NFI technical regulations specify that "mixed leaf forest" is included within the needleleaf forest area. This two-level constraint defines the mapping used to identify potential forest pixels by harmonizing corresponding forest classes from diverse LULC products, while ensuring that the reconstructed forest area and the areas of our derived PFTs are strictly consistent with their corresponding NFI statistical areas.

3.~~1~~ 2 ~~Interpolation~~ Extrapolation and interpolation of NFI statistical data

~~For the construction of the 1980–2023 forest cover time series, the provincial-level forest area from each NFI period was assigned to the final year of that period (e.g., data from the 1973–1976 survey were assigned to the year 1976) (Yue et al., 2024). Given the non-uniform time intervals of the NFI data and the potential for non-linear trends in provincial forest area, cubic spline interpolation was employed. This piecewise method constructs a series of cubic polynomials between data points and ensures continuity in the first and second derivatives, making it well-suited to handling non-uniform intervals whilst providing a high-quality fit and smooth trend lines. Cubic spline interpolation was used to infill missing forest area data for the period 1976–2021, whilst the Holt-Winters exponential smoothing method was applied to forecast data for 2022 and 2023. Owing to provincial-level differences in policy and other influencing factors, the interpolation and forecasting were performed independently for each province (Fig. S1).~~

~~For Hong Kong, Macau, and Chongqing, comprehensive statistical data were only available from 2003 onwards, which necessitated data extrapolation for the period 1980–2002. Linear regression was used to estimate the historical forest area for these regions, adopting a methodology similar to that of Yu et al. (2022) and Yue et al. (2024) (Fig. S1). To mitigate the uncertainty inherent in this approach, the extrapolated values were not used directly to define the historical forest extent (e.g., Fig. S1, Chongqing). Instead, the forest area value from the consistency-level raster (see Sect. 3.2) that most closely matched the extrapolated estimate was identified, and its corresponding spatial extent was used as the forest mask for that year.~~

To construct the continuous forest cover time series for 1981–2023, provincial forest areas from each NFI period were assigned to the final year of that period (e.g., data from the 1976–1981 survey were assigned to 1981) (Yue et al., 2024). However, due to the latency in NFI data publication, the temporal coverage of statistical data varies by category: statistics for wooded land, needleleaf forests, and broadleaf forests are available only up to the eighth inventory (2013); arbor forest statistics up to the ninth inventory (2018); and total forest area up to the tenth inventory (2023). To address these data gaps, we extrapolated the missing values for the post-2013 period using linear regression models based on published data. This approach is supported by prior studies indicating that national afforestation targets exhibit a consistent linear trend over time, increasing by approximately 1.8 million hectares annually (He et al., 2024; Xu et al., 2023).

Specifically, we first modeled the relationship between provincial total forest area and arbor forest area using available data from 2003–2018. We applied these models to extrapolate the arbor forest area for 2023, using the known 2023 total forest area as the predictor (Fig. S1; China $R^2 = 0.97$). Concurrently, using data from 2003–2013, we established linear regression models between total forest area and wooded land area to preliminarily predict wooded land areas for 2018 and 2023. According to the definition in Sect. 3.1, the area of wooded land must strictly equal or exceed that of arbor forest. However, a comparison of our preliminary 2018 wooded land predictions with the recorded 2018 arbor forest data revealed logical inconsistencies in Tibet and Gansu provinces, where the predicted wooded land area was smaller than the arbor forest area. To rectify this, we adjusted the 2018 wooded land values for these two provinces to match their actual arbor forest areas and re-incorporated these corrected data into the model to predict the 2023 wooded land area. A final consistency check of the 2023

predictions revealed a similar discrepancy in Qinghai province, which was adjusted accordingly to match the predicted arbor forest area (Fig. S2; China $R^2 = 0.98$).

Next, to estimate the needleleaf and broadleaf forest areas for 2018 and 2023, we assumed that the growth trends observed during 2003–2013 persisted into the 2013–2023 period (Chini et al., 2021). Given that arbor forest area is the sum of needleleaf and broadleaf forest areas (Sect. 3.1), we calculated the ratio of each forest type to the total arbor forest area for 2003, 2008, and 2013. We then built linear regression models based on these historical ratios to project the corresponding proportions for 2018 and 2023. The final provincial areas for needleleaf and broadleaf forests were derived by multiplying these projected ratios by the (known or extrapolated) arbor forest areas for 2018 and 2023. Finally, once the areas for all benchmark years were established, we applied linear interpolation to fill the annual data gaps between these benchmarks (Yu et al., 2022; Yue et al., 2024). All extrapolation and interpolation procedures were performed independently for each province to account for regional heterogeneity in policies and environmental factors. It should be noted that arbor forest statistics are missing for Hong Kong, Macau, and post-2013 Taiwan. As China's major afforestation programmes do not cover these regions, we did not reconstruct the arbor forest areas for Hong Kong, Macau, or post-2013 Taiwan (Zhang et al., 2025).

3.~~2~~ 3 Forest cover reconstruction

~~Rather than adopting traditional biophysical definitions of "forest" (e.g., canopy cover ≥ 10%, tree height ≥ 5 m) or adhering to a single classification standard from the FAO or national bodies, this~~ This study developed a data-driven "forest consistency" method to reconstruct historical forest cover (Fig. 1). The method involved overlaying all available LULC datasets for each year (Fig. ~~S2~~S3). For any given pixel, "consistency" (CON) was defined as the number of datasets that classified it as forest (Fig. ~~S3a~~S4a). A pixel was subsequently identified as a "potential forest pixel" if it was classified as forest in at least one dataset (i.e., $CON > 0$). The consistency value was then used to establish priority, whereby a higher CON value indicated a greater likelihood of the pixel representing true forest cover (Xia et al., 2023; Fang et al., 2020).

To determine the consistency threshold for the final forest classification, all potential forest pixels were ranked in descending order of their CON value. The NFI-derived area for a given province was used as the target value to establish this threshold. Specifically, two scenarios were considered. First, if the total area of all potential forest pixels were less than the NFI-reported area, all potential pixels were classified as forest, a scenario which could result in an underestimation for that province. Second, if the total area of potential pixels exceeded the NFI-reported area, a cumulative summation was performed. Pixels were incrementally summed, starting from the highest consistency value downwards, until the cumulative area bracketed the NFI target area (A_{NFI}). If the cumulative area of pixels with $CON \geq m$ was less than A_{NFI}, but the cumulative area of pixels with $CON \geq m - 1$ exceeded A_{NFI}, then m was defined as the consistency threshold. All pixels with a consistency value $\geq m$ were subsequently classified as forest. To precisely match the NFI target area, however, a portion of the remaining required area was fulfilled by selecting pixels from the $CON = m - 1$ level. Based on the assumption that, within a given consistency level, a higher NDVI value indicates a greater likelihood of forest cover, the ~~maximum~~ growing-season NDVI was calculated for all pixels at the $CON = m - 1$ level. These pixels were then ranked in descending order of their NDVI

value. The top n pixels were subsequently selected as "residual forest pixels", where n was determined by the remaining area required to precisely match the NFI target.

In summary, the final forest classification identified pixels exhibiting both high cross-dataset consistency and high growing-season NDVI values. The total area of this final classification was strictly constrained by provincial NFI statistics, thereby ensuring the reconstructed maps align with the authoritative inventory data. While this method generally ensures a close correspondence to the NFI-reported area, a minor systematic underestimation can occur. This is a consequence of pixel resolution limitations, particularly when the final area required to meet the NFI target is smaller than that of a single pixel.

3.~~3~~ 4 PFT dataset development

3.~~34~~.1 Distinguishing between needleleaf and broadleaf forest types

Theoretically, the same reconstruction method used for total forest cover could be applied to directly classify ~~four~~ five distinct PFTs: evergreen needleleaf, evergreen broadleaf, deciduous needleleaf, ~~and~~ deciduous broadleaf ~~forests~~, and mixed leaf forests. However, data availability constraints preclude the direct application of this method, since few LULC products offer this level of thematic detail, particularly for periods before 1990. For instance, for the year 1985, only a single available dataset differentiated between needleleaf and broadleaf forests, while for ~~1980~~1981, no dataset provided phenological classifications (i.e., evergreen vs. deciduous, Table S1). Consequently, a foundational assumption of this study is that the relative spatial distribution of these ~~four~~ five PFTs remained static over the analysis period.

Extrapolation and interpolation of the NFI~~The NFI~~ provides provincial-level forest area statistics for needleleaf and broadleaf forests for the period 1981–~~2013~~2023, but it lacks phenological classifications (i.e., evergreen vs. deciduous). Therefore, the initial classification step in this study was to distinguish between needleleaf and broadleaf forests within the previously reconstructed total forest extent.

To achieve this, ~~seven~~ nine LULC products containing forest type information were selected (Table S1). All available temporal layers from these ~~seven~~ nine products, amounting to ~~73~~ 92 distinct data layers in total, were subsequently overlaid. Based on~~Adhering to~~ the previously stated assumption of a static PFT distribution, these ~~73~~ 92 layers were used to generate two static consistency maps: one for needleleaf and one for broadleaf forests (Fig. ~~S4~~S5). To ensure close spatial correspondence between this PFT classification and the main forest cover dataset, the static consistency maps were masked using the annual 1 km forest extent maps reconstructed in the previous step. This process generated annual consistency maps for each forest type, constrained within the total forest area for each respective year.

A critical preliminary step was required to adapt the main reconstruction method for distinguishing between needleleaf and broadleaf forests. The primary goal of this step was not to produce a final classification, but to resolve conflicts among the source LULC datasets. This ensured that each pixel could be assigned a single, spatially exclusive 'type-specific consistency' value, which is a prerequisite for the reconstruction logic that follows.

To achieve this, two consistency values were calculated for each pixel: needleleaf consistency (CON_{need}), representing the number of LULC datasets classifying the pixel as needleleaf forest; and broadleaf consistency (CON_{broa}), representing the number of datasets classifying it as broadleaf forest. A rule-based approach was then applied to handle the three possible scenarios and assign a preliminary, exclusive status to each pixel:

1. Both consistency values are non-zero ($CON_{need} > 0$ and $CON_{broa} > 0$): The pixel's consistency type was determined by comparing the two values. If $CON_{need} > CON_{broa}$, the pixel was designated as a needleleaf consistency pixel. If $CON_{need} < CON_{broa}$, it was designated as a broadleaf consistency pixel. If $CON_{need} = CON_{broa}$, the pixel was flagged as 'ambiguous', and its classification was deferred to a later stage.

2. Only one consistency value is non-zero (e.g., $CON_{need} > 0$ and $CON_{broa} = 0$): The pixel was designated as a consistency pixel of the corresponding forest type for which the value existed.

3. Both consistency values are zero ($CON_{need} = 0$ and $CON_{broa} = 0$): The pixel was provisionally flagged as "unclassified forest type" in this step, with its final status to be determined later.

The second major step was to generate annual distribution masks for needleleaf and broadleaf forests for each province for the period 1981–~~2013~~2023. This was achieved by integrating provincial NFI area statistics with ~~the type~~type-specific consistency information. In a process analogous to the total forest cover reconstruction, the NFI area statistics for needleleaf and broadleaf forests were used as annual targets. The specific allocation logic, which uses NDVI data as a secondary criterion, depended on the relationship between the consistency-derived area and the NFI target area. This resulted in three distinct cases:

1. Both forest types have "valid" consistency data (i.e., the total potential area from the consistency map exceeds the NFI target area). In this scenario, the allocation method described previously was applied independently to each type. The consistency threshold (m) was determined, and the remaining area required to meet the NFI target was fulfilled by selecting pixels from the $CON = m - 1$ level, ranked in descending order of their growing-season NDVI value.

2. Only one forest type has "valid" consistency data. The "valid" type was processed first, following the same procedure as in Case 1. For the "invalid" type (where the potential area was less than the NFI target), a hierarchical sourcing strategy was used to fulfill its NFI area target. Pixels were drawn sequentially from the following pools, using the NDVI-ranking method for selection at each stage:

First, from pixels flagged as "ambiguous" ($CON_{need} = CON_{broa}$).

Second, from a pixel pool generated using the "valid" type's unallocated pixels. This involved using the "remainder" pixels from the "valid" type's consistency map (i.e., those not selected to meet its own NFI target) to mask the original consistency map of the "invalid" type. From this newly masked map, pixels were then selected in descending order of their consistency value until the NFI area target for the "invalid" type was fulfilled.

Third, from pixels flagged as an "unclassified forest type".

3. Neither forest type has "valid" consistency data. In this case, both NFI area targets were fulfilled by drawing pixels exclusively from the "ambiguous" and "unclassified forest type" pools. The allocation was prioritized for the provincially

"dominant" type (i.e., the type with the larger NFI area). Once its target was met, the remaining pixels from these pools were allocated to the other forest type. The NDVI-ranking method was used for all selections.

Finally, this process resulted in the output of annual needleleaf and broadleaf forest distribution masks for the specified period.

3.~~3~~4.2 Distinguishing ~~between~~ evergreen, ~~and~~ deciduous, and mixed leaf forest ~~phenological~~ types

In a process analogous to the classification of needleleaf and broadleaf types, a further classification was performed to distinguish ~~between~~ evergreen, ~~and~~ deciduous, and mixed leaf forest types ~~phenologies~~. This step ~~utilized~~utilised a new set of consistency rasters that classified pixels based on both compositional and phenological type (Fig. ~~S5~~S6). However, as the NFI dataset lacks area statistics for these ~~phenological~~ subtypes, no area-based constraints could be applied. Instead, the classification was performed directly within the masks delineated in the previous step. For example, evergreen and deciduous broadleaf~~needleleaf~~ forests were identified from within the total broadleaf~~needleleaf~~ mask based solely on their respective consistency values. An identical operation was performed for ~~broadleaf~~ needleleaf forests. Notably, as the area of mixed forest is included within the needleleaf forest (see Sect. 3.1), mixed forest is also identified from the total needleleaf forest mask. Any pixel within a given life-form mask (i.e., needleleaf or broadleaf) that could not be assigned a ~~phenological~~ subtype was designated as a "residual" pixel (e.g., "residual needleleaf") and reserved for subsequent processing.

The previously generated consistency masks were then used to refine the ~~phenological~~ classification within the needleleaf and broadleaf categories. This was achieved through a pixel-level comparison of type-specific consistency values. The process is illustrated below using the example of distinguishing the composition within needleleaf forests:~~between deciduous broadleaf forest (DBF) and evergreen broadleaf forest (EBF).~~

~~1. Pixel has competing classifications: Where a pixel possessed a non-zero consistency value for both deciduous (CON_{DBF}) and evergreen (CON_{EBF}) broadleaf types, a direct comparison was made:~~

~~If $CON_{DBF} > CON_{EBF}$, the pixel was classified as DBF. If $CON_{DBF} < CON_{EBF}$ the pixel was classified as EBF. If $CON_{DBF} = CON_{EBF}$, the pixel was not assigned a phenological type. Instead, it was designated as "residual broadleaf" and reserved for subsequent processing.~~

~~2. Pixel has a single classification: Where a pixel possessed a non-zero consistency value for only one phenological type (e.g., $CON_{DBF} > 0$ and $CON_{EBF} = 0$), it was classified accordingly as either DBF or EBF.~~

A comparison is made among deciduous needleleaf forest (CON_{DNF}), evergreen needleleaf forest (CON_{ENF}), and mixed leaf forest (CON_{MF}). If one value is the unique maximum, the pixel is classified as the corresponding type. However, if a tie for the maximum value exists (i.e., two or all three values are equal and maximal), the pixel is designated as "residual needleleaf forest" and reserved for subsequent processing.

The classification of evergreen and deciduous ~~needleleaf~~ broadleaf forests (~~ENF~~ EBF and ~~DNF~~DBF) followed an identical procedure to that of ~~broadleaf~~ needleleaf forests. This initial stage resulted in the annual classification of ~~four~~ five

primary PFTs (DNF, ENF, DBF, EBF, MF), alongside a category of "residual" pixels requiring further processing. This category comprised pixels confirmed as either needleleaf or broadleaf, but for which a ~~phenological~~ subtype could not yet be assigned. To resolve these pixels, two subsequent methods were employed: a ~~neighborhood~~neighbourhood analysis and an environmental inference method.

~~Neighborhood~~Neighbourhood ~~Analysis~~analysis: For each "residual" pixel, a 10×10 pixel ~~neighborhood~~neighbourhood window was established, a size selected in alignment with previous studies performing neighbourhood analysis at similar scales (Harper et al., 2023). ~~around it.~~ Within this window, the total number of pixels belonging to each of the ~~four~~ five classified PFTs (DNF, ENF, DBF~~, and~~ EBF, and MF) was counted. The classification logic was then applied as follows:

For a "residual needleleaf pixel", the counts of DNF, ~~and~~ ENF, and MF ~~neighbors~~neighbours were compared. The pixel was classified as the category with the maximum number of neighbours. If the counts for two or three types were equal (and maximal), or if no classified needleleaf neighbours existed within the window, the pixel was labeled as "pending". ~~If the DNF count was greater, the pixel was classified as DNF. Conversely, if the ENF count was greater, the pixel was classified as ENF. If the DNF and ENF counts were equal, or if no classified needleleaf neighbors were present in the window, the pixel was flagged as "pending".~~ An identical logic was applied to "residual broadleaf" pixels, based on the counts of their DBF and EBF ~~neighbors~~neighbours.

Environmental ~~Inference~~ inference ~~Method~~method: For the small number of remaining "pending" pixels (typically those with no classified ~~neighbors~~neighbours), an environmental inference method was used to assign a final subtype~~phenology~~ based on climatic and topographic data (see Sect. 2.4). The procedure involved the following steps: First, the climate zone and topography data were overlaid to create a map of unique "environmental strata" (i.e., unique combinations of climate and topography). Second, for each province and year, the relative proportion of the ~~four~~ five PFTs was calculated within each unique environmental stratum. Third, a "pending" ~~broadleaf~~ needleleaf pixel was assigned the ~~phenological~~ subtype ~~(EBF or DBF)~~ that was most prevalent within its specific environmental stratum, according to the calculated proportions. The same logic was applied to "pending" ~~needleleaf~~ broadleaf pixels.

Finally, the classifications from all steps were merged to produce the annual distribution maps for the ~~four~~ five PFTs (DNF, ENF, DBF, ~~and~~ EBF, and MF) for each province.

3.~~3~~4.3 Final PFT classification

Adopting the methodology of Bonan et al. (2002) and utilising the historical climate data (see Sect. 2.4), the five ~~four~~ preliminary forest types were further subdivided into ~~eight~~ nine final PFTs. The specific climatic variables used for this classification are detailed in Table 2 and include:

T_c is the mean temperature of the coldest month.

GDD (Growing Degree Days) are the annual cumulative temperature exceeding a 5°C baseline.

The daily growing degree days (GDD_d) are calculated as follows:

$$GDD = \sum_{d=1}^{365} \max(T_d - T_b, 0) \quad (14)$$

Where:

T_d is the mean daily temperature, and T_b is the base temperature for growth, set at 5°C

Since we used the monthly mean temperature data for 1981–2023 published by Peng et al. (2019a)daily mean temperature data are not available in the ERA5-Land product, an alternative method was employed to estimate GDDGDD. This involved substituting the monthly mean temperature for T_d in Eq. (14) and then multiplying the result by the number of days in that month to yield a monthly GDDGDD value. The annual GDDGDD was subsequently calculated as the sum of these monthly values. We utilised the annual GDD and T_c values for each year during the 1981–2023 period to reflect the year-to-year dynamic changes in climatic conditions.

Through the sequence of methods detailed above, a comprehensive historical dataset of forest cover for China, classified by PFT, was produced.

Table 2. Classification scheme for deriving plant functional types (PFT) from forest life forms and climatic rules.

Plant functional type	Forest type	Climate rules
Temperate evergreen needleleaf forest	Evergreen needleleaf forest	T_c > -19°C and GDD > 1200
Boreal evergreen needleleaf forest	Evergreen needleleaf forest	$T_c \leq$ -19°C or $GDD \leq$ 1200
Deciduous needleleaf forest	Deciduous needleleaf forest	none
Tropical evergreen broadleaf forest	Evergreen broadleaf forest	T_c > 15.5°C
Temperate evergreen broadleaf forest	Evergreen broadleaf forest	$T_c \leq$ 15.5°C
Tropical deciduous broadleaf forest	Deciduous broadleaf forest	T_c > 15.5°C
Temperate deciduous broadleaf forest	Deciduous broadleaf forest	-15°C < $T_c \leq$ 15.5°C and GDD > 1200
Boreal deciduous broadleaf forest	Deciduous broadleaf forest	$T_c \leq$ -15°C or $GDD \leq$ 1200

3.4 5 Accuracy assessmentValidation

The accuracy of the reconstructed forest cover maps was validated using independent field survey data. The validation was conducted in two stages: first for needleleaf and broadleaf forest types, and subsequently for the total forest area. Two primary sources of data were used for this validation. The first was the global all-season sample set from Li et al. (2017), the first of its kind, developed from Landsat-8 data. Generated through visual interpretation in Global Mapper software, this global dataset contains approximately 340,000 training samples (~90,000 locations) and 140,000 validation samples (~36,000 locations). For the present study, a subset was selected, comprising forest samples from 2014 and 2015 within the study area. Additionally, samples from land types commonly confused with forest (e.g., cropland and grassland) were aggregated into a single "non-forest" category. This process yielded 1,412 forest and 2,591 non-forest samples from this source. The second source was a nationwide field survey conducted between 2011 and 2013, which recorded plot-level details including vegetation type. From this field campaign, 2,860 independent validation samples for needleleaf and broadleaf forest types were obtained, comprising 1,433 broadleaf and 1,427 needleleaf forest samples. Combining these sources resulted in a final validation dataset of 6,863

~~independent samples (Fig. S6). This dataset was used to generate confusion matrices and calculate overall accuracy (OA), user's accuracy (UA), producer's accuracy (PA), and the F1-score for the reconstructed maps.~~

To validate the accuracy of our reconstructed annual PFT maps, we collected an extensive validation dataset covering the entire study area. Our validation points were labeled based on three data sources: (1) ground plots from the NFI conducted between 2009 and 2013. For each plot, the dataset provides the plot ID, geographic coordinates, and its classification into one of five forest types: ENF, EBF, DNF, DBF, and MF. (2) a collection of Landsat images spanning 1985–2023 (Cai et al., 2025), and (3) high-resolution imagery from Google Earth. First, to assess the temporal consistency of the NFI ground plots, we applied the normalised burn ratio (NBR) (García and Caselles, 1991) to the dense Landsat time series at these plot locations. NBR is calculated as: $(NIR - SWIR)/(NIR + SWIR)$. This index is recognised for its sensitivity in detecting forest disturbances within Landsat time series (Perbet et al., 2024; White et al., 2022). We then employed the Landsat-based detection of trends in disturbance and recovery (LandTrendr) algorithm (Kennedy et al., 2010) to examine the stability of the 1 km grid cells surrounding these nationwide samples from 1985 to 2023. LandTrendr is a widely used disturbance detection method designed to detect anomalies and trends in time series, distinguishing between abrupt and gradual changes (Kennedy et al., 2018; Cheng et al., 2023). We implemented this algorithm in GEE to distinguish between stable (which remained unchanged between 1985–2023) and unstable (which underwent a change in at least one year during 1985–2023) samples among the NFI ground plots and to identify the timing of any detected changes. This process yielded 5,481 stable and 1,229 unstable sample points, which were then assigned to their respective years within the 1981–2023 period to form the validation database.

Following the good practice guidelines for sample size decisions proposed by Olofsson et al. (2014), we used a proportional stratified sampling design to randomly draw validation samples from the validation database for each year, stratified by the five PFT classes: ENF, EBF, DNF, DBF, and MF. Each annual validation set consisted of approximately 1,280 points. For the proportionally rare classes (DNF and MF), the sample size was increased to 100 points (Fig. S7) to reduce the standard error of the accuracy estimates for these less common categories. The PFT class of each sample was further confirmed through visual interpretation of high-resolution imagery available on Google Earth. This labeling was conducted by ten experts experienced in remote sensing data analysis. We organized multiple training sessions for these experts to ensure adherence to a consistent sample labeling protocol. When a decision was difficult, the sample point was submitted for a collective team discussion, and the final reference label was assigned only after a unanimous consensus was reached. Based on these validation samples, we generated a confusion matrix for each year and calculated the producer's accuracy (PA), user's accuracy (UA), overall accuracy (OA), and the F1-score:

$$PA_k = \frac{p_{kk}}{\sum_{j=1}^{m} p_{kj}} \quad (5)$$

$$UA_k = \frac{p_{kk}}{\sum_{i=1}^{m} p_{ik}} \quad (6)$$

$$OA = \sum_{k=1}^{m} p_{kk} \quad (7)$$

$$F1 = \frac{2 \times PA \times UA}{PA + UA} \times 100\% \quad (8)$$

Where p_{kk} is the area proportion of class k that is correctly classified (i.e., class k in both the reference data and the map); $\sum_{j=1}^{m} p_{kj}$ represents the total area proportion of class k in the reference data (the row sum); $\sum_{i=1}^{m} p_{ik}$ represents the total area proportion of class k in the classified map (the column sum); and m is the number of land cover types. We then corrected the accuracy estimates based on map uncertainties and calculated the corresponding standard errors and 95% confidence intervals (Olofsson et al., 2014). We also conducted a cross-validation with existing annual land cover products (ESA CCI, MCD12Q1, and GLC_FCS30D) that include five PFT classes (ENF, EBF, DNF, DBF, and MF) to better evaluate the quality of the dataset reconstructed in this study.

In addition to this sample-based validation, an indirect accuracy assessment was performed by analys~~z~~ing the consistency among the input LULC datasets. This approach is pertinent as the final product is an integration of these sources. Here, consistency is defined at the pixel level as the number of LULC datasets that concur on the classification of a specific forest type. The underlying assumption of this analysis is that a higher consistency value for a given pixel indicates greater confidence in its classification and a higher likelihood of it being correct (Xia et al., 2023).

3.~~5~~ 6 Forest change analysis

Forest change is defined as the transition of land cover between forest and non-forest states over a given period. It is typically classified into change events (i.e., forest gain or loss) and stable states (i.e., persistent forest or persistent non-forest) (Winkler et al., 2021). Forest gain represents a transition from a non-forest to a forest state, while forest loss is the reverse process (Hansen et al., 2013). To identify the onset year and duration of forest change events across China for the period ~~1980~~1981–2023, a pixel-level ~~time series~~time series analysis was developed based on the annual forest mask sequence.

This methodology is illustrated here using the detection of forest gain. First, the annual forest masks were standardized into binary values (0 = non-forest; 1 = forest) to create a spatiotemporal data cube. For this analysis, a "stable" forest state was defined as a pixel remaining as forest for at least ~~three~~ five consecutive years ~~(Yang and Song, 2023)~~. The onset year of a forest gain event was then identified for each pixel as the first year it transitioned from a non-forest state to a stable forest state.

Following the identification of a gain event, the duration of forest persistence was calculated. This duration is the number of years from the onset of the gain until either: (a) the pixel underwent a stable loss event, defined as transitioning to non-forest and remaining so for at least ~~three~~ five consecutive years, or (b) the end of the study period (2023) if no such loss event occurred. The detection of forest loss events and their duration followed the inverse logic.

This analysis produced four maps: two indicating the onset year for forest gain and loss events, and two representing the duration of these respective periods.

3.6 7 Modelling assessment using LPJ-GUESS Modelling assessment

~~The impact of the new PFT distribution on surface fluxes was assessed using LPJ–GUESS (Lindeskog et al., 2021), a process-based DGVM. The primary objective of the simulation was to evaluate how the updated PFT map influences key carbon and water fluxes at the land surface.~~

~~To isolate the effect of the PFT distribution, two distinct model experiments were conducted. Both experiments were driven by identical climate forcing data from the ERA5–Land reanalysis product (including temperature, precipitation, and downward shortwave radiation) for the period 1981–2013. The crucial difference between the experiments was the PFT input map:~~

~~EXP1 utilised the new PFT map developed in this study.~~

~~EXP2 utilised the global PFT dataset from ESA CCI as a baseline for comparison.~~

~~In both experiments, the PFT distribution from the year 2010 was applied cyclically for each year of the simulation to maintain a static land cover driver. The LPJ–GUESS model was run at a 0.1° × 0.1° spatial resolution. The simulation period was 1981–2013; model outputs before 1981 were considered part of the "spin-up" phase and were discarded from the analysis.~~

~~The outputs from the two experiments were compared for the China region across a range of land surface variables, including gross primary productivity (GPP), net ecosystem exchange (NEE), leaf area index (LAI), and actual evapotranspiration (ET). As the PFT map was the sole variable altered between the two experiments, any observed differences in the output fluxes could be directly attributed to its influence.~~

The impact of the new PFT distribution on surface fluxes was assessed using LPJ–GUESS (Lindeskog et al., 2021), a process-based DGVM. The model was driven by China meteorological forcing data (CMFD 2.0) (He et al., 2020) at a 0.1° resolution for the 1951–2023 period, which includes daily averages of temperature, incoming shortwave radiation, and precipitation. The data are publicly available from the National Tibetan Plateau Data Center at: https://doi.org/10.11888/Atmos.tpdc.302088 (last access: 24 September 2025). Atmospheric CO_2 concentrations followed historical trajectories (Friedlingstein et al., 2024). Gridded monthly nitrogen deposition data (0.5° resolution) were also supplied as input (Lamarque et al., 2013), using the nearest grid cell value for each simulation grid. Soil properties—namely the fractions of sand, silt, and clay; organic carbon content; C:N ratio; pH; bulk density; and organic carbon density—were derived from the China dataset of soil properties for land surface modelling version 2 (CSDL v2) dataset (Shi et al., 2025). This database, generated using advanced integrated machine learning algorithms from multiple representative historical soil profiles and high-resolution environmental covariates, provides 0.1° maps at six soil layers across China. The data are publicly available at: https://www.scidb.cn/s/ZZJzAz (last access: 23 September 2025). We averaged the soil texture data over 0–200 cm and resampled all soil inputs to align with the meteorological forcing grid.

The LPJ-GUESS model was run at a 0.1° × 0.1° spatial resolution. Vegetation structure and its associated carbon, water, and nitrogen pools were initialized using a 500-year spin-up phase (starting from bare ground) by cycling 1951–1980 detrended meteorological data. This was followed by the historical simulation from 1981–2023. To account for natural disturbances, a

disturbance interval of 100 years was set, and the GlobFirm wildfire sub-model (Thonicke et al., 2001) was enabled. To ensure the model's capability to simulate Chinese forest ecosystems, key parameters related to photosynthesis, autotrophic respiration, and plant water use efficiency were manually adjusted after benchmarking (all updated PFT parameters are summarized in Table S3).

To isolate and quantify the independent impact of PFT distribution, we designed three distinct model experiments. During the 1981–2023 period, all three experiments were driven by the same climate forcing data and consistent model parameters. The sole difference among experiments was the PFT input map: EXP1: utilised the new PFT map developed in this study. EXP2: utilised the global PFT dataset from ESA CCI (Harper et al., 2023). EXP3: utilised the global PFT dataset from MCD12Q1 (Sulla-Menashe et al., 2019). In all three experiments, we cycled the 2010 PFT distribution to maintain a static land cover driver. We simulated the monthly total GPP, NEE, LAI, and ET for 2010, focusing our comparison on the mean differences between the PFT datasets during the summer (June–August) to highlight primary changes. As the PFT distribution map was the sole variable altered between experiments, any observed differences in output fluxes can be directly attributed to its influence. To assess the plausibility of these changes, the simulation results were also compared against four remote sensing and observation-based products: FLUXCOM GPP, FLUXCOM NEE, GIMMS LAI4g, and GLEAM ET. All observational products were resampled to 0.1° resolution using bilinear interpolation to match the LPJ–GUESS simulation grid.

4 Results

4.1 Accuracy assessment of the reconstructed ~~forest cover~~PFT dataset

~~Validation based on field survey data from five time points shows that for the total forest classification, the overall accuracy in 2014 and 2015 was 94.79 ± 0.49% and 95.74 ± 0.53%, respectively, while the user's accuracy for forest types in these two years was 93.65 ± 0.81% and 94.11 ± 1.06%, respectively (Table 3). For the period 2011–2013, the overall accuracy for needleleaf forests ranged between 84.35 ± 1.6% and 90.18 ± 2.3%, while for broadleaf forests, the range was 85.41 ± 1.5% to 92.02 ± 2.16%. The F1 score for broadleaf forests was slightly higher than for needleleaf forests (Table 4).~~ Independent validation based on five forest types for the period 1981–2023 demonstrates that the accuracy of the PFT dataset reconstructed in this study is both stable and satisfactory. The overall accuracy (OA) ranged from 79.74% to 88.5%, with a mean OA of 84.86% ± 1.18% (Fig. 2f). Among the specific forest classes, EBF achieved the highest mean F1-score (93.03%), followed by ENF (92.49%), DBF (84.89%), DNF (62.29%), and MF (54.03%) class (Fig. 2a–e). Furthermore, in most years, the overall accuracy of our dataset (mean 84.86% ± 1.18%) outperformed those of ESA CCI (mean 83.47% ± 1.15%), MCD12Q1 (mean 61.17% ± 1.36%), and the global 30m land-cover dynamics monitoring dataset (GLC_FCS30D) (mean 78.92% ± 1.24%) (Fig. 2f). For the classes with larger areal proportions, such as DBF, EBF, and ENF, the F1-scores of our dataset also demonstrated superior and more stable performance compared to those of ESA CCI, MCD12Q1, and GLC_FCS30D (Fig. 2a–e). This independent validation confirms the high spatial accuracy of the reconstructed PFT data in comparison to prominent existing datasets. Moreover, the temporal coverage of the dataset reconstructed in this study spans 43 years (1981–2023), exceeding

that of ESA CCI (1992–2020), MCD12Q1 (2001–2023), and GLC_FCS30D (1985–2022). ~~We also found that the reconstructed broadleaf forests exhibited higher consistency than the needleleaf forests (Figure S3b, S3c). Notably, according to our methodology, a pixel-weighted average over the 1980–2023 period indicates that approximately 6.9% of pixels in the reconstructed needleleaf forests and 2.7% in the reconstructed broadleaf forests did not fall within their corresponding consistency type.~~Analysis of the consistency between our reconstructed PFT dataset and the input LULC datasets revealed that the reconstructed broadleaf forests exhibited higher consistency than the needleleaf forests (Fig. S4b–f), indicating higher confidence in the reconstructed BF results. Among the five PFT types, the confidence ranking from highest to lowest was DBF, EBF, ENF, DNF, and MF (Fig. S4b–f). Furthermore, according to our methodology, a pixel-weighted average over the 1981–2023 period indicates that fewer than 1% of pixels for all five reconstructed PFT types did not fall within their corresponding consistency type (the specific proportions were 0.50% for DBF, 0.10% for EBF, 0.03% for DNF, 0.01% for ENF, and 0.05% for MF, Fig. S8).

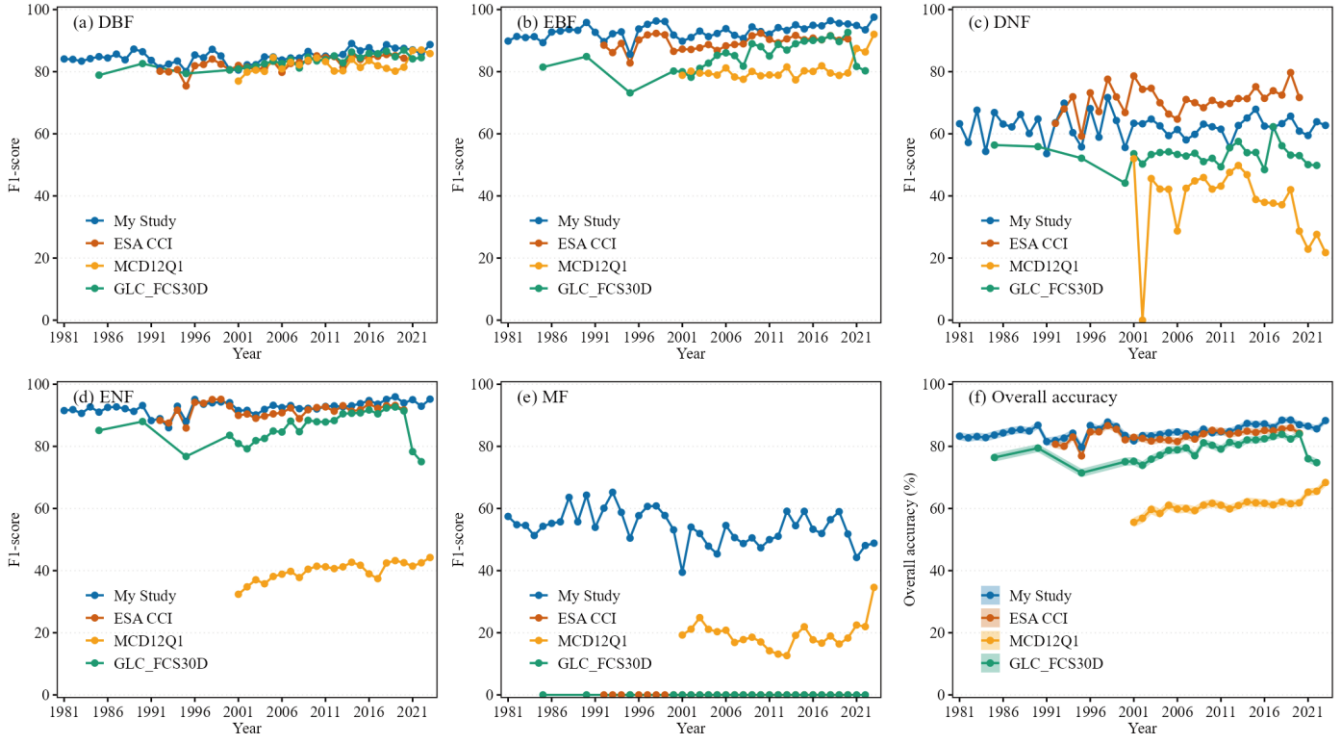

Figure 2. F1-scores and overall accuracies (OA) of our dataset (This study), the European Space Agency Climate Change Initiative land cover (ESA CCI) dataset, the Moderate Resolution Imaging Spectroradiometer land cover (MCD12Q1) dataset, and the global 30m land-cover dynamics monitoring dataset (GLC_FCS30D), validated against national forest inventory (NFI) field plots. The shaded area in (f) represents ±1 standard error.

~~**Table 3.** Confusion matrix for the reconstructed total forest cover classification for 2014 and 2015.~~

~~Classification~~			

Year	Reference	Forest	Non-forest	User's Accuracy (%)	Producer's Accuracy (%)	F1 Score (%)	Overall Accuracy (%)
2014	Forest	841	72	93.65±0.81	92.11±0.89	92.88	94.79±0.49
2014	Non-forest	57	1508	95.44±0.52	96.36±0.47	95.9	
2015	Forest	463	36	94.11±1.06	92.79±1.16	93.44	95.74±0.53
2015	Non-forest	29	997	96.52±0.57	97.17±0.52	96.84	

Table 4. Confusion matrices and accuracy metrics for the needleleaf and broadleaf forest classifications for the period 2011–2013.

Year	Reference	Classification		User's Accuracy (%)	Producer's Accuracy (%)	F1 Score (%)	Overall Accuracy (%)
		broadleaf	needleleaf				
2011	broadleaf	420	90	87.32±1.52	82.35±1.69	84.76	85.41±1.5
2011	needleleaf	118	407	90.24±1.4	77.52±1.82	83.4	84.35±1.6
2012	broadleaf	644	98	92.4±1	86.79±1.24	89.51	89.93±1.11
2012	needleleaf	115	642	93.18±0.96	84.81±1.31	88.8	89.19±1.18
2013	broadleaf	170	11	91.89±2.01	93.92±1.78	92.9	92.02±2.16
2013	needleleaf	27	118	95.93±1.79	81.38±3.24	88.06	90.18±2.3

The internal consistency of the reconstructed total forest cover was assessed at ten specific time points: 19801981, 1985, 1990, 1995, 2000, 2005, 2010, 2015, 2020, and 2023 (Fig. 23). The number of inputs LULC datasets available for the reconstruction varied at each time point, with 45, 67, 56, 67, 911, 1011, 911, 910, 1012, and 4–6 products used for each respective year. The analysis showed that for each of the ten time points, 87.395.7%, 70.893.5%, 82.991.8%, 69.885.3%, 40.166.7%, 23.754.9%, 24.055.7%, 25.657.9%, 24.655.4%, and 35.285.4% of the reconstructed forest pixels, respectively, achieved the maximum possible consistency score. Conversely, pixels with the lowest possible consistency ($CON = 1$) consistently accounted for a small fraction of the total reconstructed forest area, ranging from 0.01% to 6.90.26% across different years (Fig. 23). Spatially, areas with lower forest consistency were predominantly located in the arid and semi-arid regions of northwestern China (e.g., Xinjiang, Qinghai, Ningxia) and the highly fragmented landscapes of the eastern coastal plains (e.g., Tianjin, Shandong, Jiangsu, Shanghai). In contrast, high-consistency forest areas were mainly concentrated in regions with extensive and stable forest cover, primarily in southern and central China, including provinces such as Hubei, Zhejiang, Guangxi, Guizhou, Yunnan, and Jiangxi (Fig. S9S6 and S7). A comparison and analysis of the NFI data with the forest area estimates reconstructed in this study at the provincial scale (Fig. S10) shows a good match for multiple years (1981–2023), with an R^2 close to 1 and a p-value < 0.001. This indicates that the reconstructed data from this study is highly consistent with the NFI statistics in terms of overall trends.

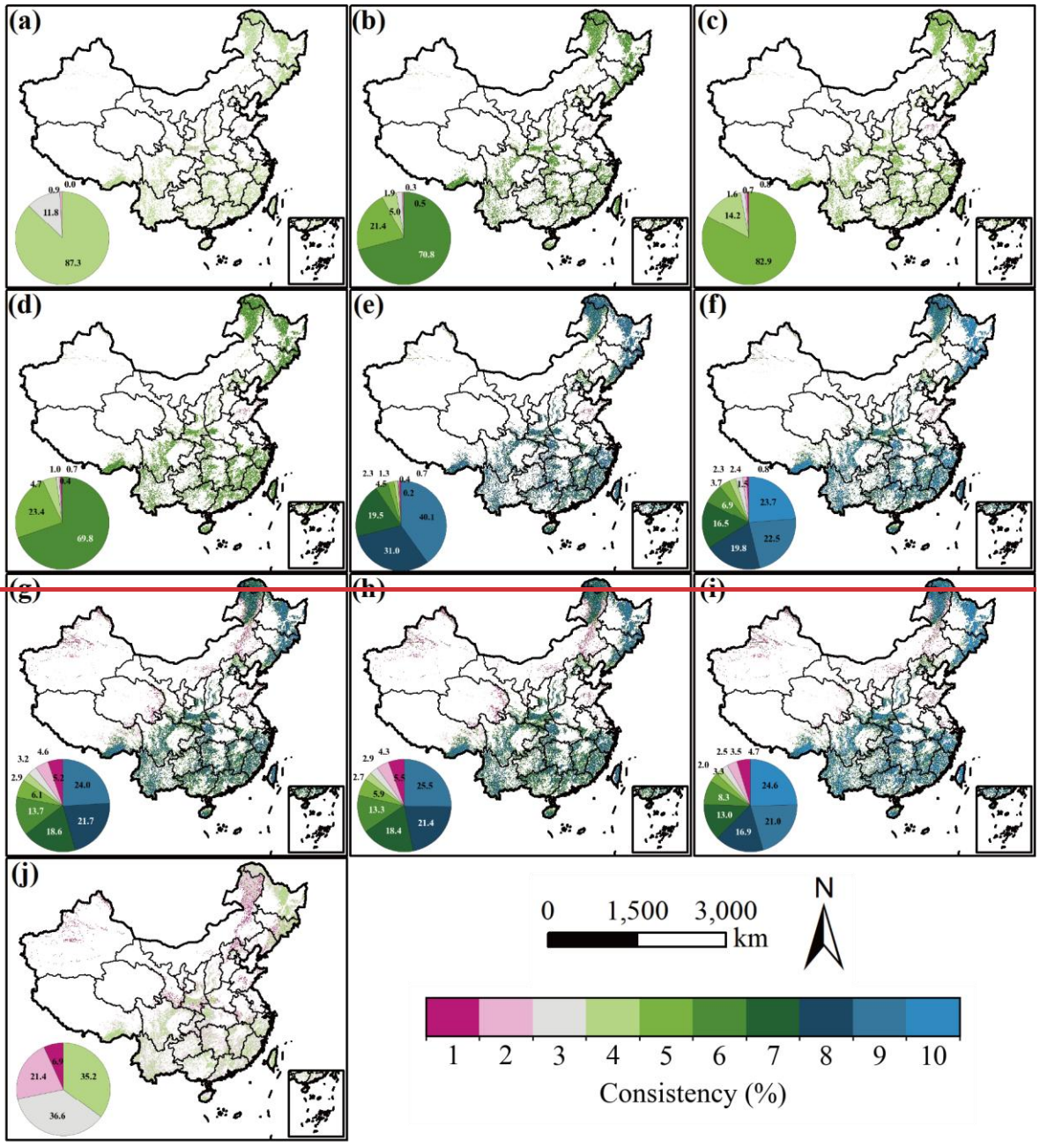
(a)
(b)
(c)
(d)
(e)
(f)
(g)
(h)
(i)
(j)
0 1,500 3,000
km
N
1 2 3 4 5 6 7 8 9 10
Consistency (%)

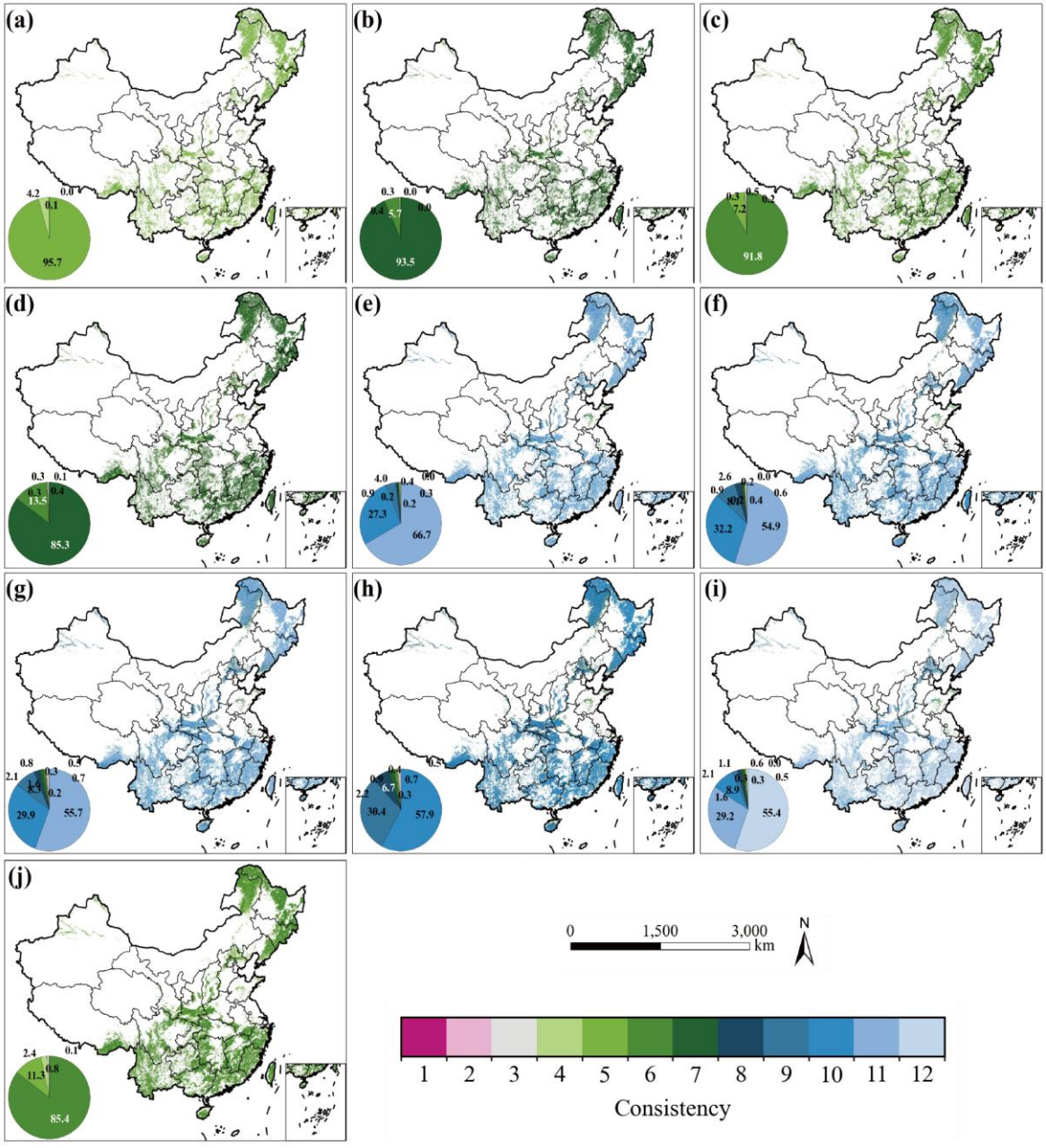

Figure ~~2~~3. The spatial distribution of reconstructed forest cover is presented at five-year intervals from ~~19801~~1981–2023 **(a)** ~~19801~~1981, **(b)** 1985, **(c)** 1990, **(d)** 1995, **(e)** 2000, **(f)** 2005, **(g)** 2010, **(h)** 2015, **(i)** 2020, **(j)** 2023, along with corresponding cross-product consistency scores. The reconstruction for each time point was compared against an ensemble of data products sourced externally (n = ~~4~~5, ~~6~~7, ~~5~~6, ~~6~~7, ~~9~~11, 1~~1~~0, 11~~9~~, 10~~9~~, ~~10~~12, and 4~~6~~, respectively). The inset pie chart (lower left) quantifies the areal proportion of the reconstructed forest dataset at various consistency levels, which serves as a proxy for the confidence in the resulting maps.

~~A comparison and analysis of the NFI data with the forest area estimates reconstructed in this study at the provincial scale (Fig. 3) shows a good match for multiple years (1981–2021), with an R^2 close to 1 and a p-value < 10^{-27}. This indicates that the reconstructed data from this study is highly consistent with the NFI statistics in terms of overall trends. However, at the provincial level, slight discrepancies were still observed for some provinces (e.g., Inner Mongolia, Heilongjiang, Yunnan, and Xinjiang), where the reconstructed estimates in certain years were either slightly higher or lower than the NFI data. These discrepancies show a more pronounced trend after 2013.~~

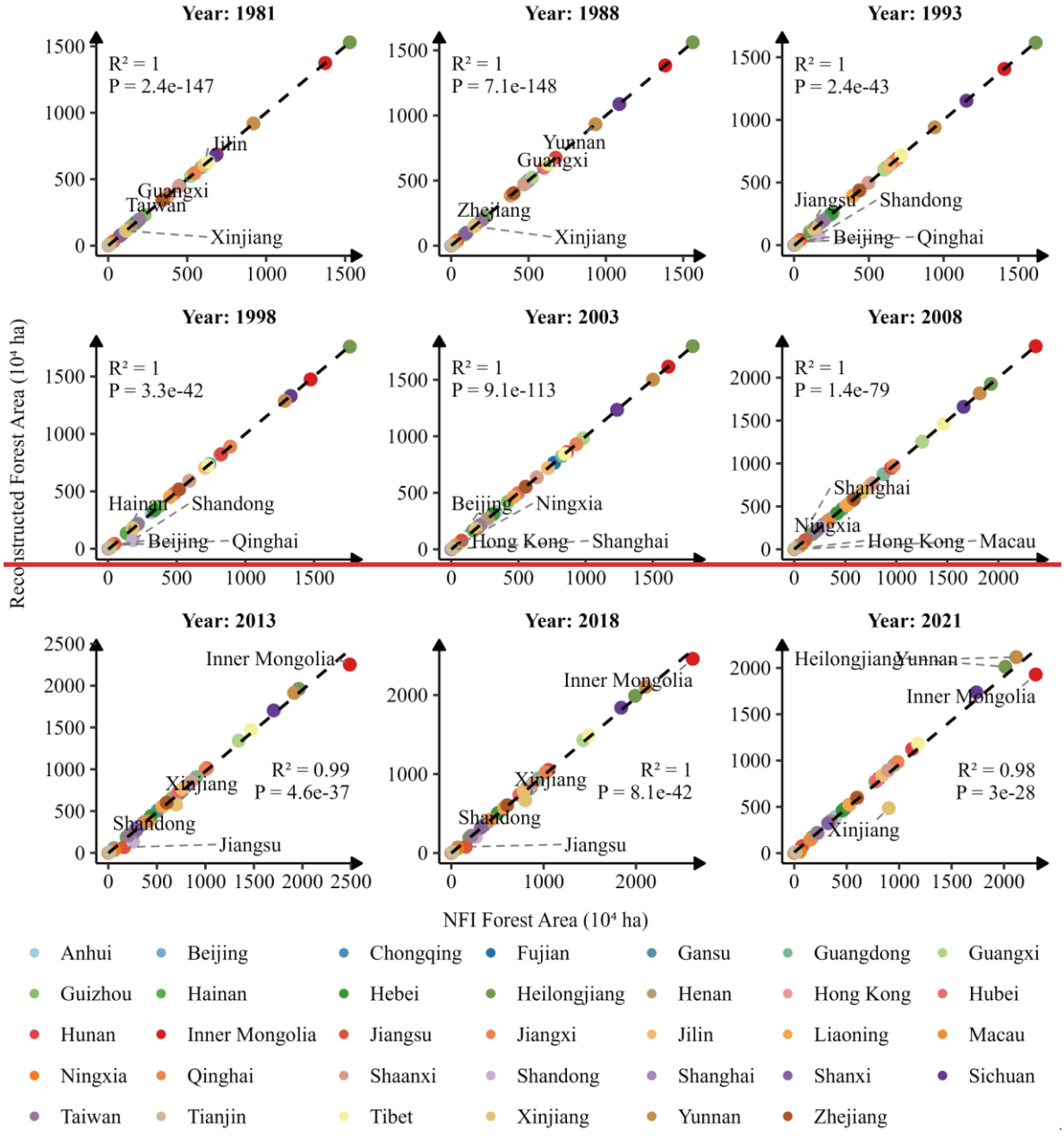

~~**Figure 3.** Scatter plot comparing provincial-level forest area as reported by NFI with estimates from the reconstructed maps of this study.~~

4.2 Spatiotemporal distribution of the reconstructed PFT dataset~~Reconstructed forest cover dataset description~~

This dataset provides annual forest cover distribution from 1981 to 2023 (Fig. 3) and the distribution of nine PFTs at a 1 km spatial resolution (Fig. 4).~~This dataset provides annual forest cover distribution from 1980 to 2023 (Fig. 2) and the distribution of eight PFTs from 1981 to 2013 at a 1 km spatial resolution (Fig. 4).~~ The data are supplied in the WGS 1984 Albers equal-area conic projection. The ~~eight~~ nine PFTs~~,~~ are: (1) boreal evergreen needleleaf forest, (2) temperate evergreen needleleaf forest, (3) temperate evergreen broadleaf forest, (4) boreal deciduous broadleaf forest, (5) temperate deciduous broadleaf forest, (6) tropical deciduous broadleaf forest, (7) tropical evergreen broadleaf forest, ~~and~~ (8) deciduous needleleaf forest, and (9) mixed leaf forest. ~~The complete dataset is openly accessible at the Zenodo repository under the DOI 10.5281/zenodo.16208012 (Liu et al., 2025, last access: 20 July 2025).~~

For the reference year ~~2013~~2023, the dataset indicates that China's forests are composed of temperate evergreen broadleaf forest (27.5%), temperate evergreen needleleaf forest (23.4%), boreal deciduous broadleaf forest (16.7%), temperate deciduous broadleaf forest (16.1%), deciduous needleleaf forest (6.6%), boreal evergreen needleleaf forest (4.4%), mixed leaf forest (4.3%), tropical evergreen broadleaf forest (0.9%), and tropical deciduous broadleaf forest (0.05%).~~evergreen needleleaf forest (26.1%), deciduous broadleaf forest (23.4%), evergreen broadleaf forest (18.1%), and deciduous needleleaf forest (6.2%).~~ Although temperate evergreen needleleaf and boreal deciduous broadleaf forests were the two largest components by area prior to 2000, their proportional contributions to the total forest area subsequently declined from 31.3% to 23.4%~~27.1% to 21.1%~~ and from 20.0% to 16.7%~~19.2% to 14.2%~~, respectively. Conversely, the proportional representation of temperate evergreen broadleaf and temperate deciduous broadleaf forests expanded, increasing from 18.5% to 27.5%~~15.3% to 17.9%~~ and from 9.5% to 16.1%~~6.4% to 8.9%~~, respectively (Fig. 4).

Spatially, the primary forest regions are concentrated in Northeast, Southeast, and Southwest China, whereas forest cover is relatively sparse in Northwest, Central, and East China. Furthermore, evergreen needleleaf and evergreen broadleaf forests are predominantly distributed across Southern China. Deciduous needleleaf forests are concentrated in the Greater Khingan Range in the northernmost part of Northeast China, while deciduous broadleaf forests are mainly located in Northeast China and the Qinling Mountains of Central China.

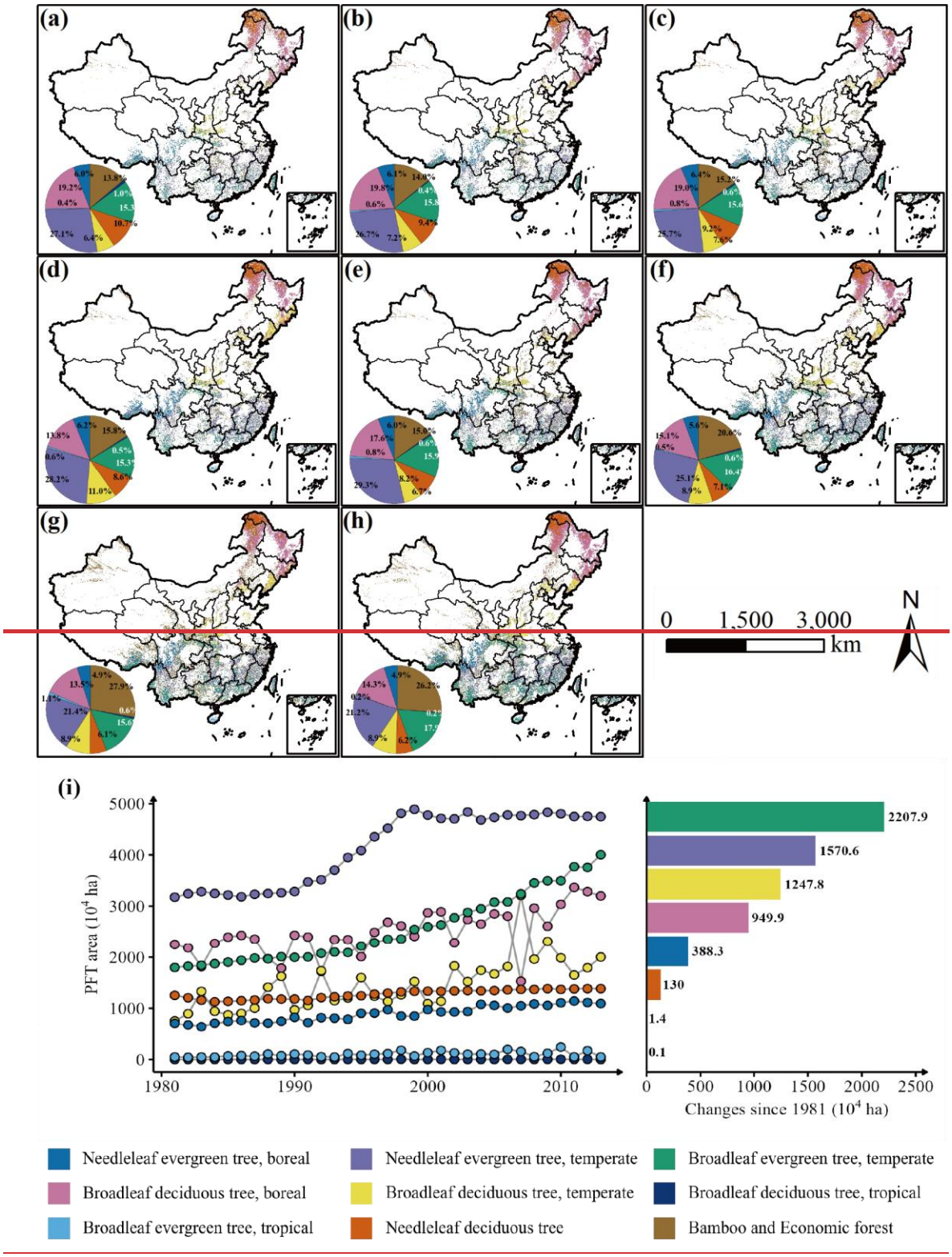
(a)
(b)
(c)
(d)
(e)
(f)
(g)
(h)
0 1,500 3,000
km
N
(i)
PFT area (10^4 ha)
5000
4000
3000
2000
1000
0
1980
1990
2000
2010
2207.9
1570.6
1247.8
949.9
388.3
130
1.4
0.1
0 500 1000 1500 2000 2500
Changes since 1981 (10^4 ha)
Needleleaf evergreen tree, boreal
Needleleaf evergreen tree, temperate
Broadleaf evergreen tree, temperate
Broadleaf deciduous tree, boreal
Broadleaf deciduous tree, temperate
Broadleaf deciduous tree, tropical
Broadleaf evergreen tree, tropical
Needleleaf deciduous tree
Bamboo and Economic forest

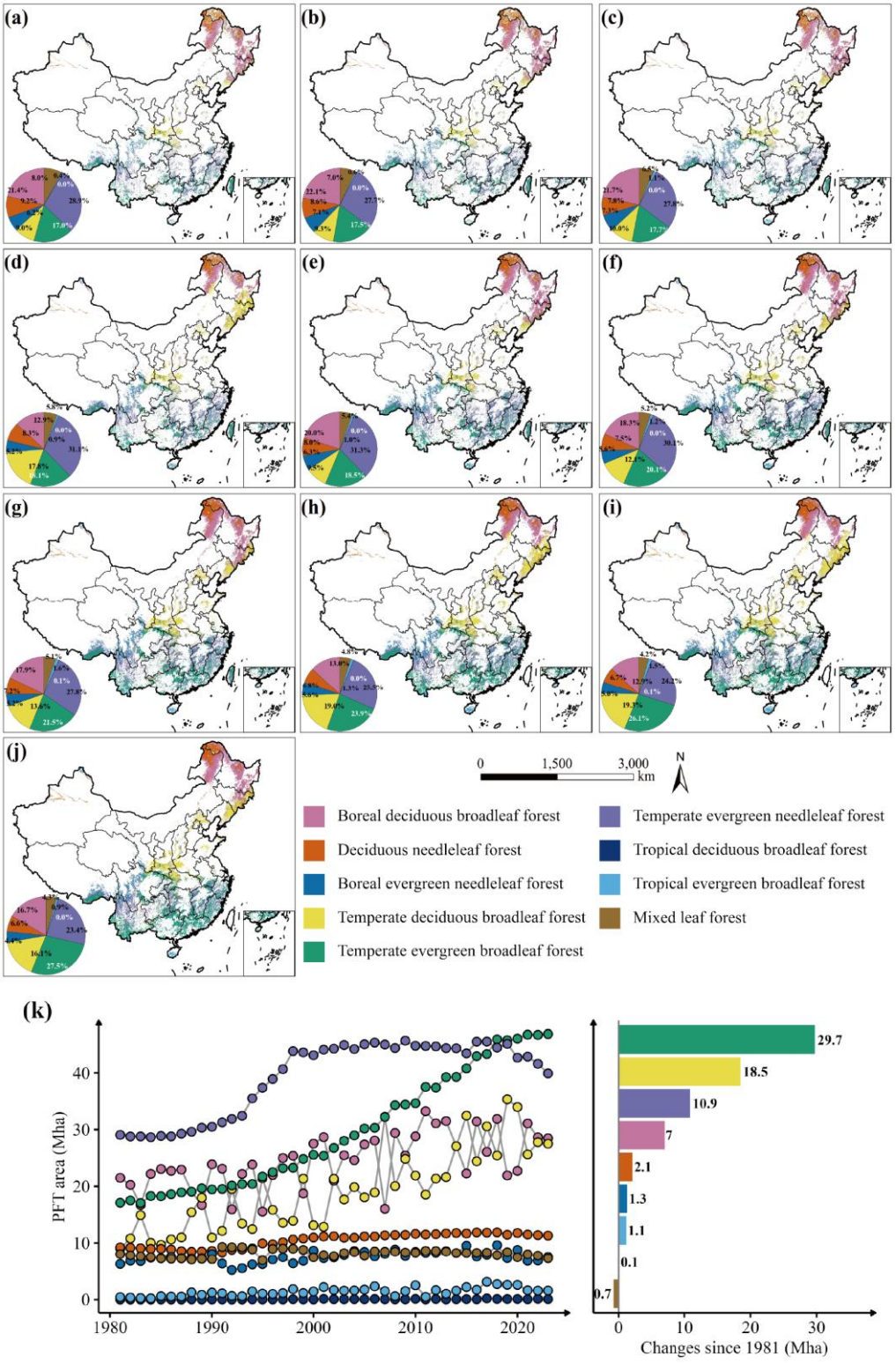
(a)
(b)
(c)
(d)
(e)
(f)
(g)
(h)
(i)
(j)
0 1,500 3,000 km
N
Boreal deciduous broadleaf forest
Deciduous needleleaf forest
Boreal evergreen needleleaf forest
Temperate deciduous broadleaf forest
Temperate evergreen broadleaf forest
Temperate evergreen needleleaf forest
Tropical deciduous broadleaf forest
Tropical evergreen broadleaf forest
Mixed leaf forest
(k)
PFT area (Mha)
1980
1990
2000
2010
2020
29.7
18.5
10.9
7
2.1
1.3
1.1
0.1
0.7
Changes since 1981 (Mha)

Figure 4. Spatial distribution patterns and area proportions of China's forest plant functional types (PFTs) for selected years between 1981 and ~~2013~~2023, **(a)-(~~h~~j)** correspond to the years 1981, 1985, 1990, 1995, 2000, 2005, 2010, ~~and 2013~~2015, 2020, and 2023, respectively;~~,~~ **(~~i~~k)** Temporal dynamics and total variation in PFTs from 1981 to ~~2013~~2023.

Regarding its temporal evolution, our reconstructed forest dataset faithfully reproduces the long-term dynamics of forest cover in China (Fig. 5). According to statistics from the NFI, China's forest cover has a mean annual growth rate of 1.75%. The reconstructed forest cover dataset reveals a substantial increase in China's total forest area from ~~117~~115.~~14~~ 28 million hectares (Mha) in ~~1980~~ 1981 to ~~213~~195.~~15~~ 45 Mha in 2023, with a peak of ~~236~~200.~~50~~ 05 Mha observed in ~~2020~~ 2018 (Fig. 5a). This represents an annualized growth rate of 1.~~82~~50%, demonstrating~~demonstrates~~ strong agreement with this national benchmark. Furthermore, our dataset accurately captures the distinct historical trajectories of two principal forest categories–broadleaf and needleleaf forests–since the 1980s (Fig. 5b and 5c). This net increase was primarily propelled by the expansion of temperate and boreal forests (Fig. 4). For example, the area of temperate evergreen broadleaf forest more than doubled between 1981 and ~~2013~~2023, increasing from 17.~~96~~ 10 Mha to ~~40~~46.~~04~~ 85 Mha (Fig. ~~4i~~4k). During this period, significant areal gains were also recorded for temperate deciduous broadleaf, temperate evergreen needleleaf, and boreal deciduous broadleaf forests.~~, and temperate deciduous broadleaf forests.~~ In contrast, absolute changes in the extent of tropical PFTs, boreal evergreen needleleaf forest, and mixed leaf forest ~~deciduous needleleaf forests~~ were minimal over the same interval (Fig. ~~4i~~4k).

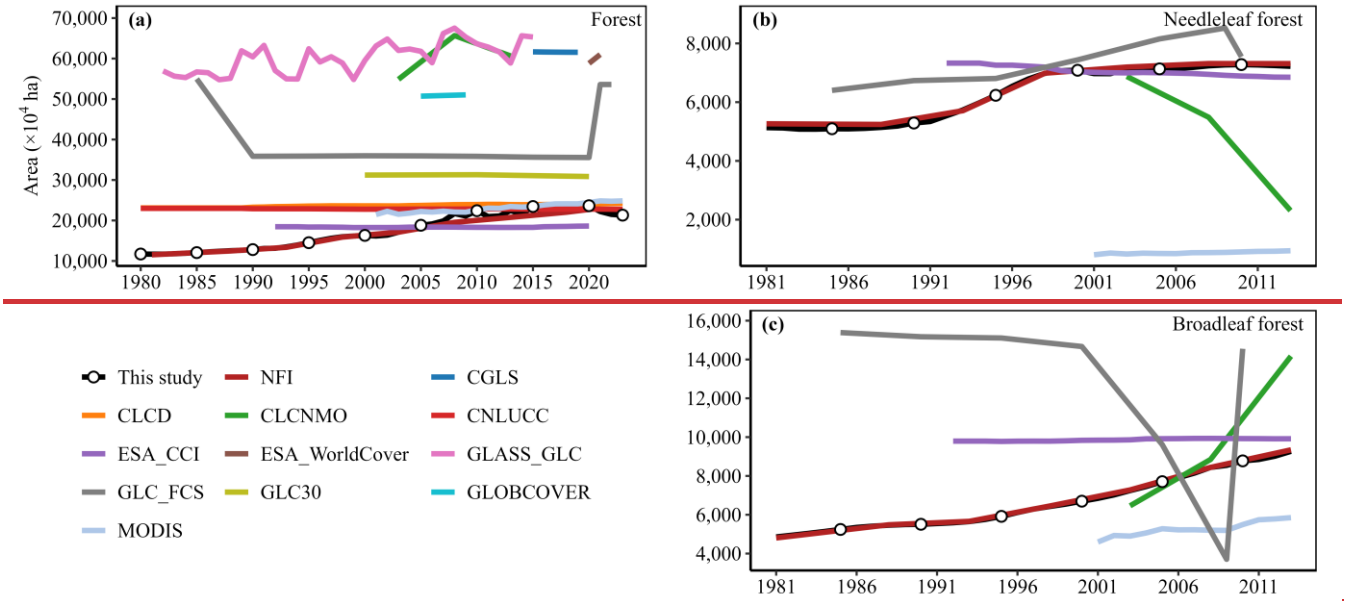

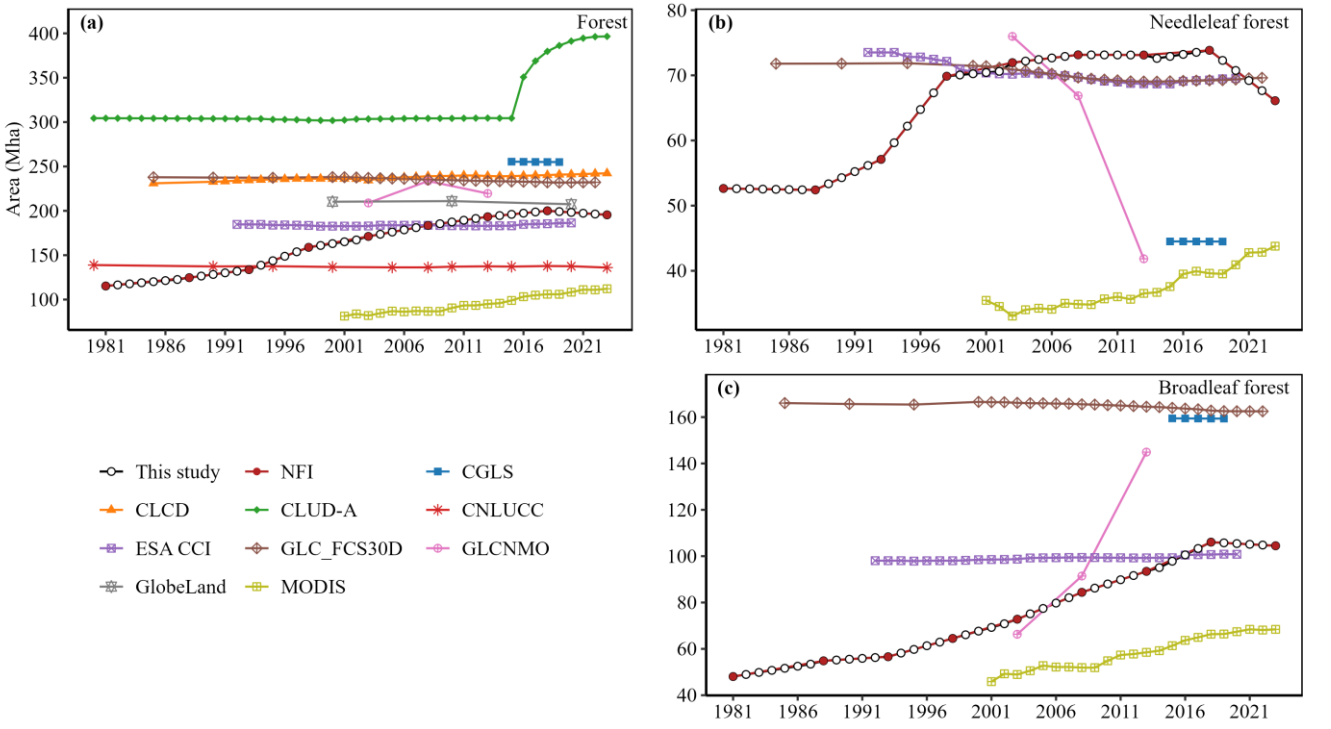

Figure 5. Temporal dynamics of national-scale total forest area, comparing the results of this study with data from national forest inventory (NFI) and other selected land use and land cover (LULC) products: **(a)** forest, **(b)** needleleaf forest, and **(c)** broadleaf forest.

4.3 Spatiotemporal patterns of forest cover change in China

Between ~~1980~~ 1981 and 2023, the total area experiencing forest change (gross change) amounted to ~~242~~166.~~11~~ 91 million hectares (Mha), equivalent to approximately ~~25~~17% of China's terrestrial surface. This comprised ~~180.53~~132.43 Mha of forest gain (~~19~~14% of the national land area) and ~~153.48~~58.69 Mha of forest loss (~~1~~6% of the national land area). Forests that remained stable, persisting from ~~1980~~ 1981 to 2023, covered ~~572.77~~62.29 Mha. This stable area represents ~~49~~54% of the total forest extent in ~~1980~~1981, implying that the remaining ~~51~~46% of the original ~~1980~~ 1981 forest cover underwent some form of change during the study period (Fig. 6q). We observed a prevalent pattern of forest change across several regions of China, characterized by a progression from more accessible areas (i.e., lower elevations near roads) to more remote locations (i.e., higher elevations far from roads). This dynamic often manifested as ~~ana~~ core-to-edge expansion of existing forest patches (Fig. 6a-p). We identified severe forest loss in the eastern Qinghai-Tibet Plateau during 1990–1996, which appears to be primarily driven by commercial logging (Chen et al., 2013). Following the implementation of large-scale ecological restoration programmes initiated in 1998—specifically the Natural Forest Protection Programme and the Grain for Green Programme—forest cover exhibited a recovery trend from 2000 to 2008 (Liu et al., 2008). Temporally, both forest loss and gain were continuous dynamic processes throughout the entire period. A prominent peak in forest turnover occurred between 1991 and ~~1993~~1996, culminating in ~~1992~~ 1994 when the combined area of gain and loss surpassed ~~35~~ 24.63 Mha. Post-~~2000~~2001, both

gain and loss ~~area~~areas exhibited a general downward trend, albeit with notable fluctuations, and moderate resurgences in turnover were observed around 2006, 2010, and 2016. Furthermore, forest loss and gain events tended to occur more concurrently (Fig. 6q). ~~A moderate resurgence in turnover was observed between 2009 and 2011, after which forest loss and gain events tended to occur more concurrently (Fig. 6q)~~.

~~Furthermore, our~~ Our analysis reveals that events of forest loss are typically of short duration (Fig. ~~S8~~S11). Over ~~35~~30% of all observed losses persisted for only 5~~3 6~~ 9 years~~, with most loss events being transient and lasting fewer than 15 years~~. In contrast, forest gain is characterized by substantially longer persistence, with a modal duration of ~~31~~25 ~~34~~ 29 years. This suggests the long-term stability of large tracts of newly established forests. The statistical distributions of persistence durations for forest gain and loss are markedly different. Loss events are predominantly concentrated in the shorter-duration intervals, whereas periods of gain are more concentrated in the medium- to long-duration brackets. This divergence indicates that newly established forests tend toward greater stability and longevity, while forest loss manifests as a more fragmented and ephemeral phenomenon.

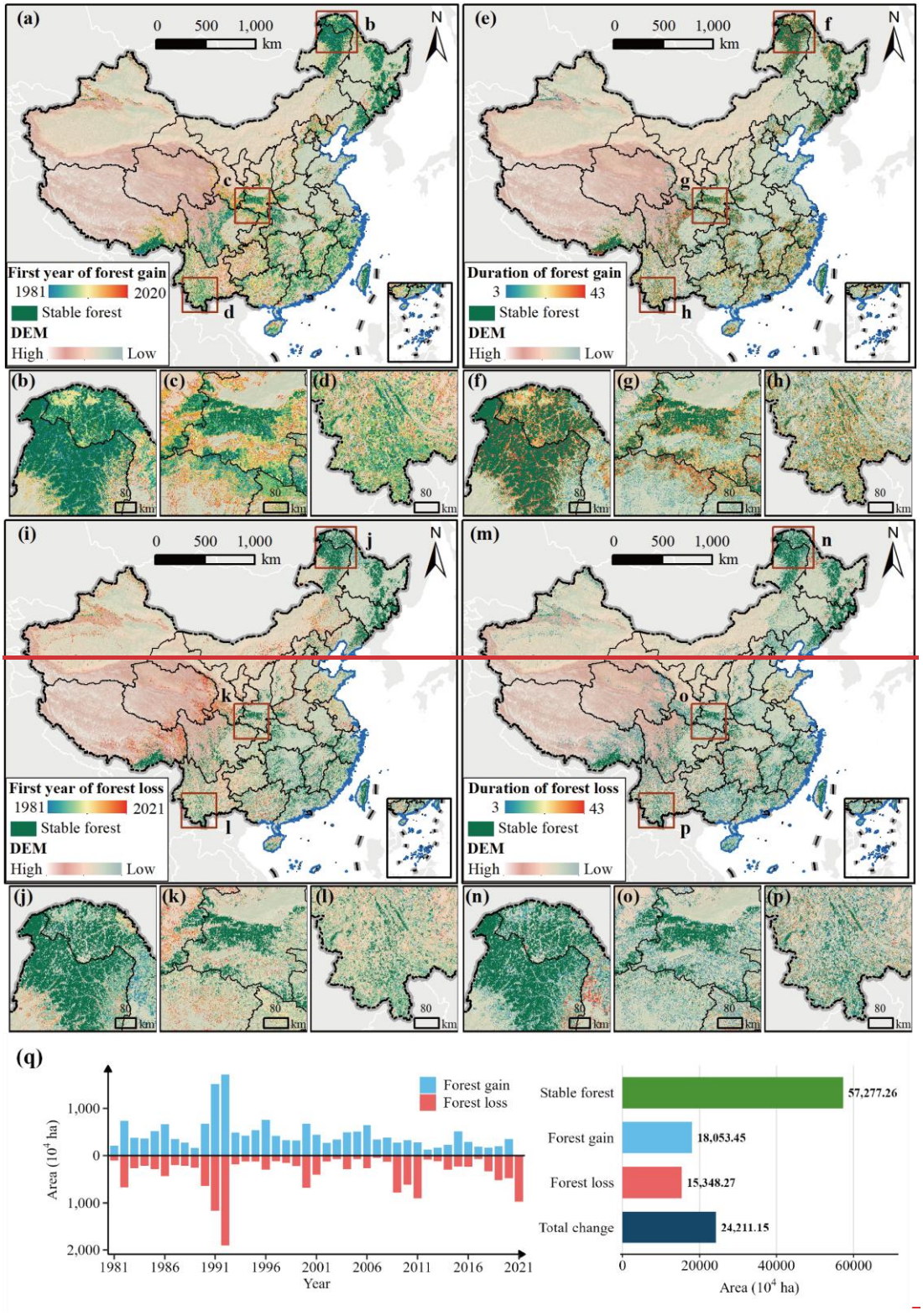
(a)
0 500 1,000 km
N
b
c
d
First year of forest gain
1981 2020
Stable forest
DEM
High Low
(e)
f
g
h
Duration of forest gain
3 43
(b)
(c)
(d)
(f)
(g)
(h)
(i)
j
k
l
First year of forest loss
Duration of forest loss
(j)
(k)
(l)
(m)
n
o
p
(n)
(o)
(p)
(q)
Forest gain
Forest loss
Area (10^4 ha)
Year
1981 1986 1991 1996 2001 2006 2011 2016 2021
Stable forest 57,277.26
Forest gain 18,053.45
Forest loss 15,348.27
Total change 24,211.15
0 20000 40000 60000
Area (10^4 ha)

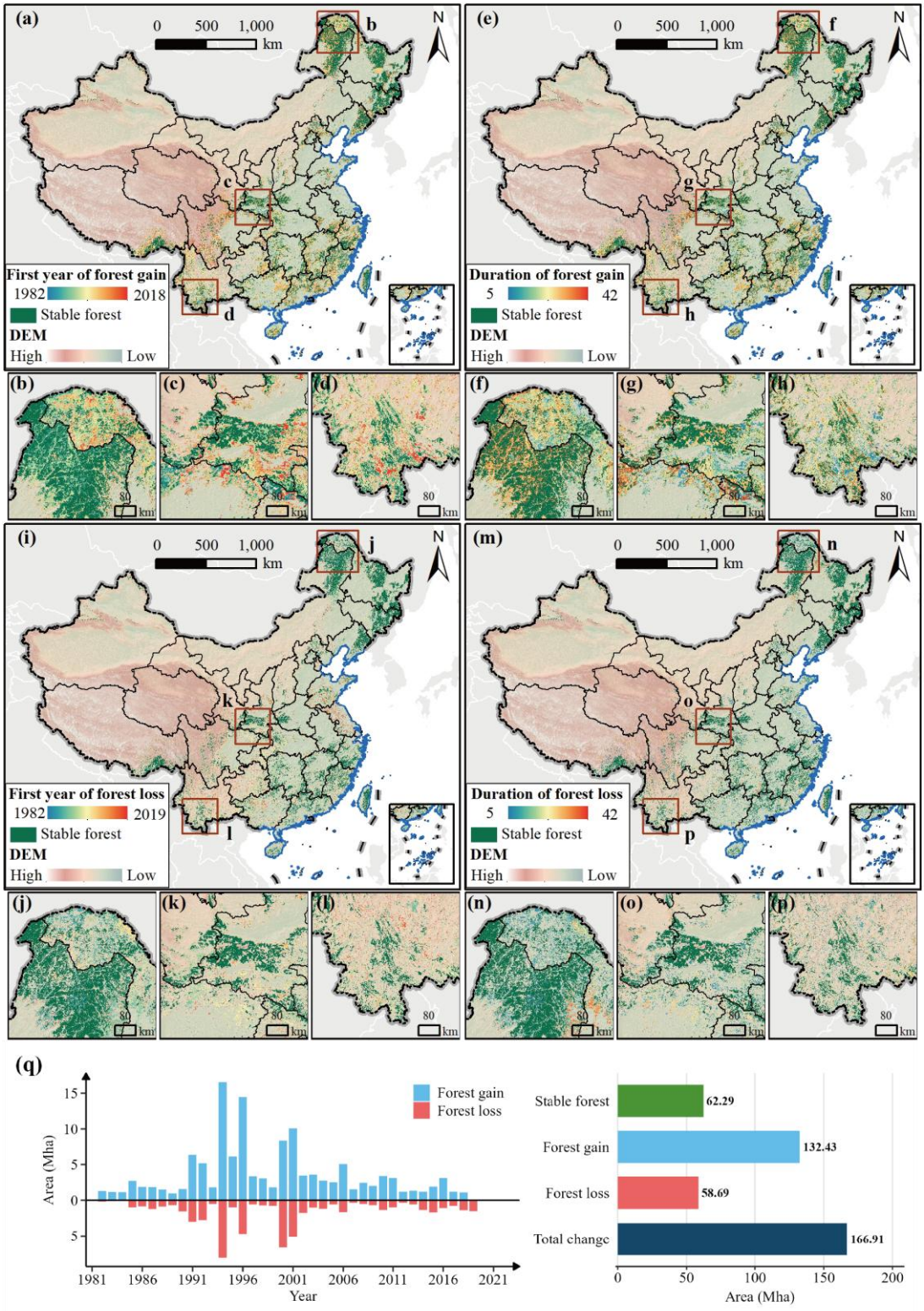
(a)
0 500 1,000 km
N
b
c
d
First year of forest gain
1982 2018
Stable forest
DEM
High Low
(e)
0 500 1,000 km
N
f
g
h
Duration of forest gain
5 42
Stable forest
DEM
High Low
(b)
(c)
(d)
(f)
(g)
(h)
80 km
(i)
0 500 1,000 km
N
j
k
l
First year of forest loss
1982 2019
Stable forest
DEM
High Low
(m)
0 500 1,000 km
N
n
o
p
Duration of forest loss
5 42
Stable forest
DEM
High Low
(j)
(k)
(l)
(n)
(o)
(p)
80 km
(q)
Forest gain
Forest loss
Area (Mha)
15
10
5
0
5
1981 1986 1991 1996 2001 2006 2011 2016 2021
Year
Stable forest
62.29
Forest gain
132.43
Forest loss
58.69
Total change
166.91
0 50 100 150 200
Area (Mha)

680

Figure 6. Spatio-temporal dynamics of forest gain and loss in China from ~~1980~~ 1981 to 2023. This figure presents: **(a-h)** the spatial patterns of forest gain, showing onset year and duration; **(i-p)** the spatial patterns of forest loss; and **(q)** the national-scale temporal dynamics, including the annual areas of forest gain and loss and a summary of total stable, gained, and lost forest areas.

4.4 LPJ–GUESS simulations: comparing the reconstructed PFT dataset against ESA CCI and MCD12Q1 ~~Modelling results~~

We assessed the impact of different PFT forcing datasets on ecosystem simulations by comparing outputs from the LPJ–GUESS model driven by our reconstructed PFT product (hereafter PFT_{local}) versus the global PFT map (PFT_{global}) from the European Space Agency (hereafter $PFT_{ESAglobal}$) and the MCD12Q1 product (hereafter $PFT_{MCD12Q1}$). The analysis, exemplified using data for the year 2010, quantifies the resulting differences in key ecosystem variables: GPP, NEE, LAI, and ET (Fig. 7). ~~While annual-scale results are also presented (Fig. S9),~~ W~~w~~e focus here on the mean differences (PFT_{local} minus PFT_{global}) during the summer period (June–August) to accentuate the primary impacts. The results indicate that the most marked divergences in simulated carbon and water fluxes are spatially coincident with regions where the ~~two~~ three products show substantial differences in the fractional coverage of tree PFTs. Regions with a higher tree cover fraction in the PFT_{local} dataset relative to $PFT_{ESAglobal}$, particularly in northeastern China (Fig. 7e, red), exhibit correspondingly elevated GPP, LAI, and ET, alongside a diminished NEE. Consequently, the resulting differentials are positive for the former variables and negative for NEE. Conversely, where the $PFT_{ESAglobal}$ dataset specifies greater tree coverage, such as in parts of southwestern China (Fig. 7e, blue), these relationships are inverted. Similarly, the comparison with $PFT_{MCD12Q1}$ yields analogous results (Fig. 8).

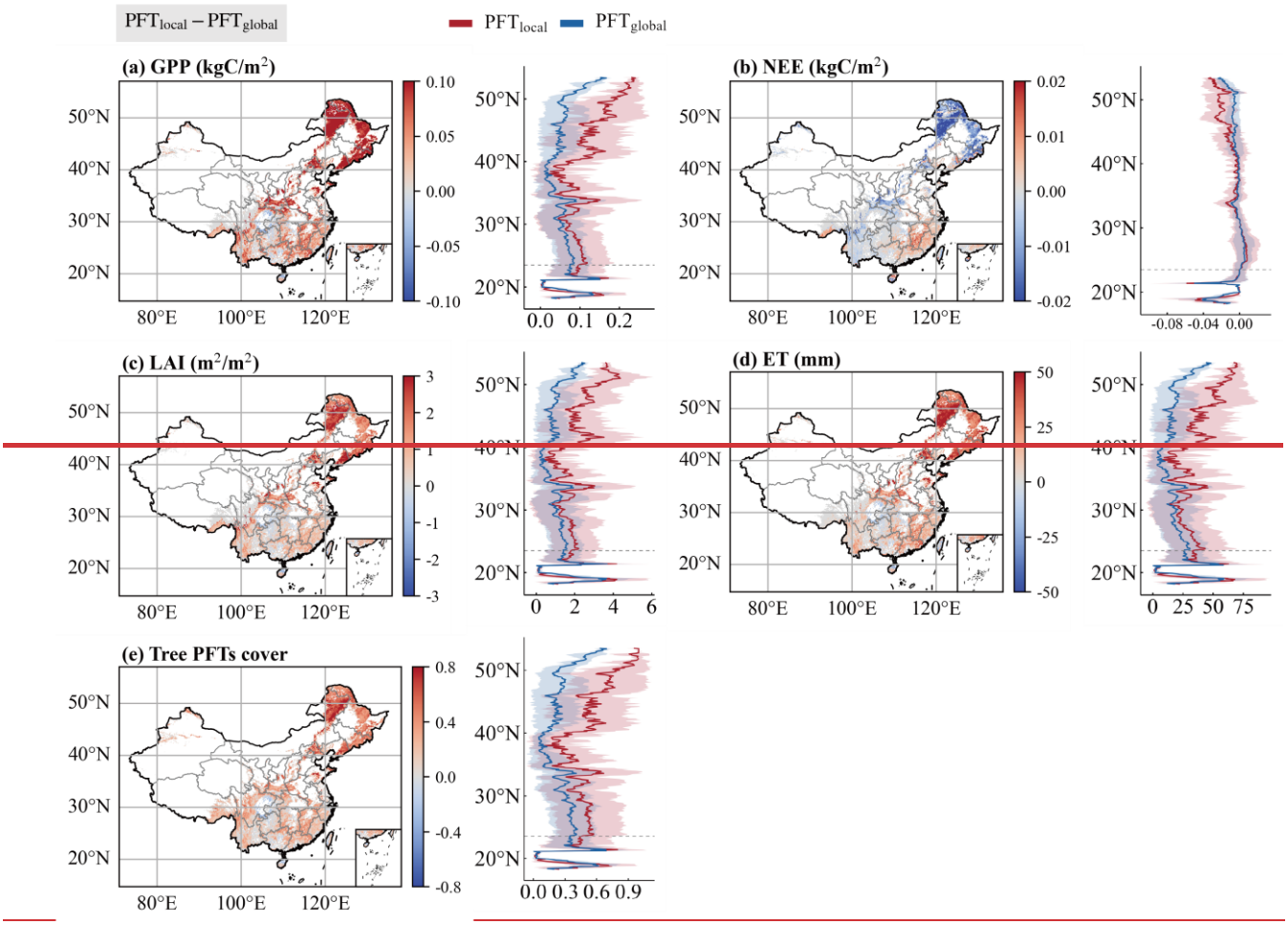
PFT$_{local}$ − PFT$_{global}$
PFT$_{local}$
PFT$_{global}$
(a) GPP (kgC/m^2)
(b) NEE (kgC/m^2)
(c) LAI (m^2/m^2)
(d) ET (mm)
(e) Tree PFTs cover
50°N
40°N
30°N
20°N
80°E
100°E
120°E
0.10
0.05
0.00
-0.05
-0.10
0.02
0.01
0.00
-0.01
-0.02
3
2
1
0
-1
-2
-3
50
25
0
-25
-50
0.8
0.4
0.0
-0.4
-0.8
0.0 0.1 0.2
-0.08 -0.04 0.00
0 2 4 6
0 25 50 75
0.0 0.3 0.6 0.9

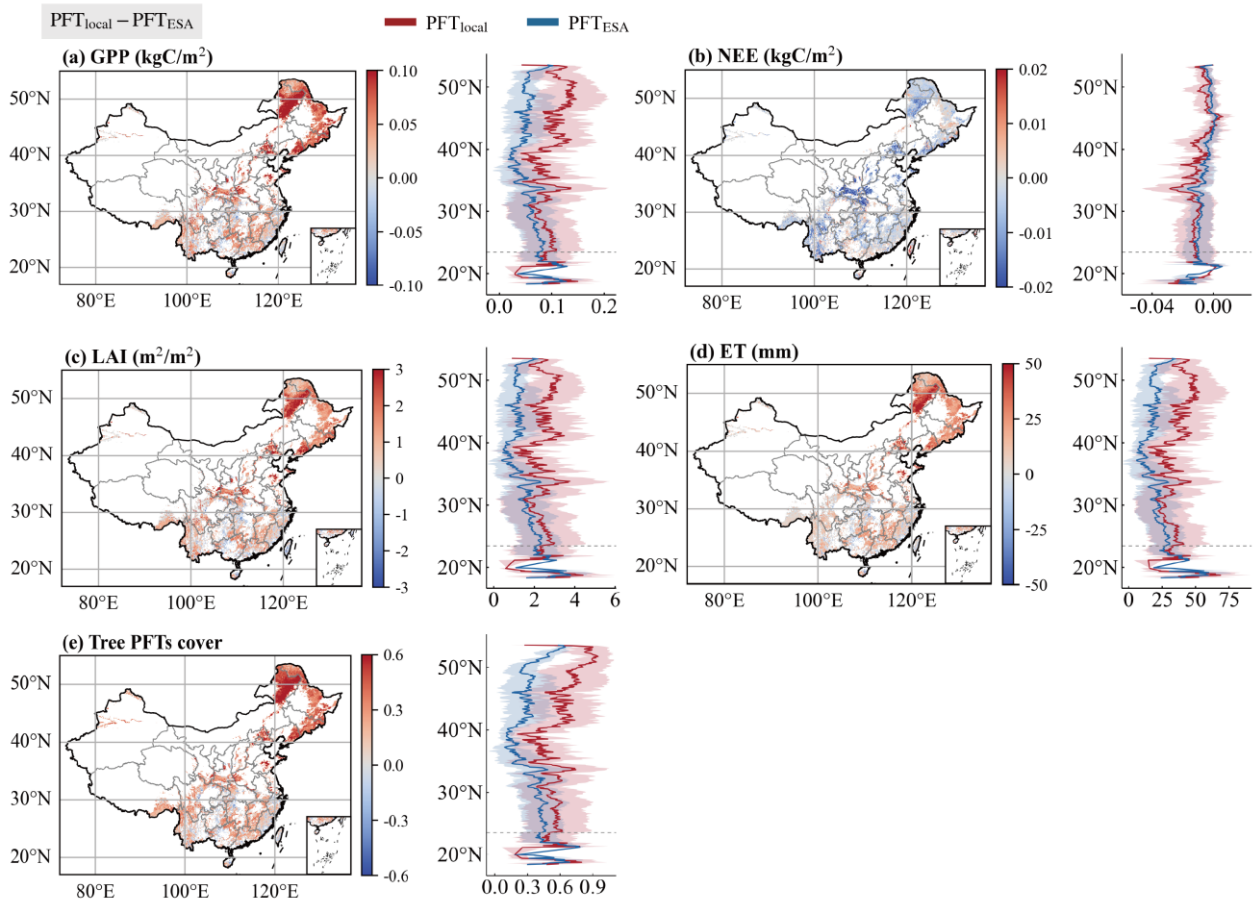

Figure 7. Comparison of Lund-Potsdam-Jena general ecosystem simulator (LPJ–GUESS) model simulations **(a–d)** and their underlying plant functional type (PFT) forcing data **(e)** for summer 2010. The comparison is made between the PFT product reconstructed in this study ($\boldsymbol{PFT_{local}}$) and the global PFT map from the European Space Agency ($\boldsymbol{PFT_{ESA}}$). The first four panels **(a–d)** show differences in simulated gross primary productivity (GPP), net ecosystem exchange (NEE), leaf area index (LAI), and actual evapotranspiration (ET). Panel **(e)** shows differences in tree PFTs cover derived directly from the input PFT maps. For all panels, the maps display the spatial difference ($\boldsymbol{PFT_{local} - PFT_{ESAglobal}}$), while the plots show the zonal mean and standard deviation for the $\boldsymbol{PFT_{local}}$ (red) and $\boldsymbol{PFT_{ESAglobal}}$ (blue) datasets individually. Note that data in panels **(a-d)** are model outputs, whereas data in panel **(e)** are from the input maps.

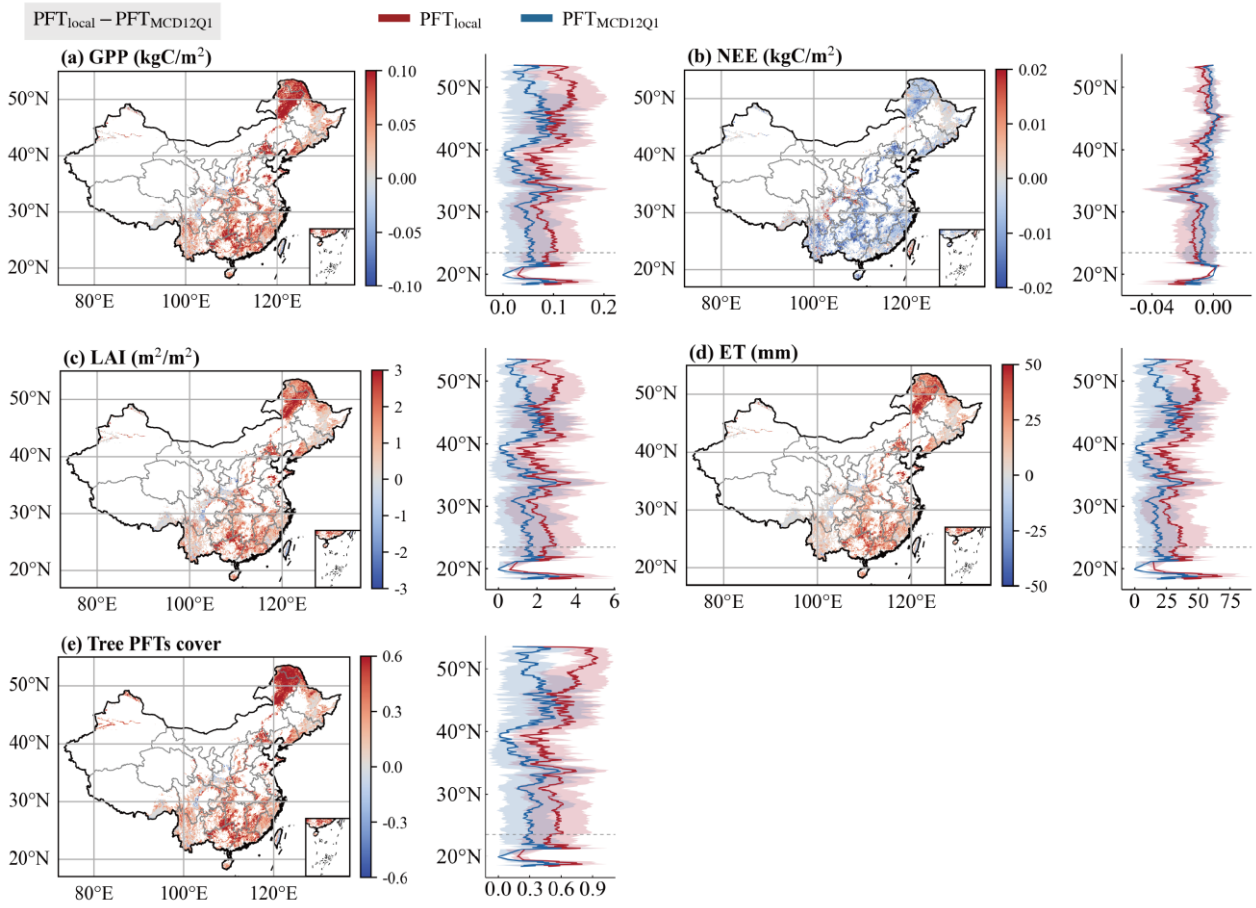

Figure 8. Comparison of Lund-Potsdam-Jena general ecosystem simulator (LPJ–GUESS) model simulations **(a–d)** and their underlying plant functional type (PFT) forcing data **(e)** for summer 2010. The comparison is made between the PFT product reconstructed in this study (PFT_{local}) and the global PFT map from the MODIS land cover type product ($PFT_{MCD12Q1}$). The first four panels **(a–d)** show differences in simulated gross primary productivity (GPP), net ecosystem exchange (NEE), leaf area index (LAI), and actual evapotranspiration (ET). Panel **(e)** shows differences in tree PFTs cover derived directly from the input PFT maps. For all panels, the maps display the spatial difference ($PFT_{local} - PFT_{MCD12Q1}$), while the plots show the zonal mean and standard deviation for the PFT_{local} (red) and $PFT_{MCD12Q1}$ (blue) datasets individually. Note that data in panels **(a-d)** are model outputs, whereas data in panel **(e)** are from the input maps.

To assess the realism of the simulations, we benchmarked the model outputs against a suite of remote sensing-based products (FLUXCOM GPP, FLUXCOM NEE, GIMMS LAI4g, and GLEAM ET), with all datasets aggregated to a common 0.1° resolution (Fig. ~~8~~ 9 for summer, June–August~~; Fig. S10 for the annual scale~~). In Fig. ~~8a~~ 9a and ~~8b~~9b, we first present a direct comparison between the surface fluxes simulated using our reconstructed PFT map (PFT_{local}) and the observational benchmarks. This baseline comparison highlights inherent discrepancies attributable to both structural biases in the LPJ–GUESS model and uncertainties within the remote sensing products themselves. Fig. ~~8c~~ 9c and 9d then isolate~~s~~ the impact of the PFT forcing by showing the change in absolute simulation error relative to the observational data. It explicitly maps areas

of improvement (demarcated in red) and degradation (in blue) in model performance when using PFT_{local} in place of $PFT_{ESAglobal}$ and $PFT_{MCD12Q1}$.

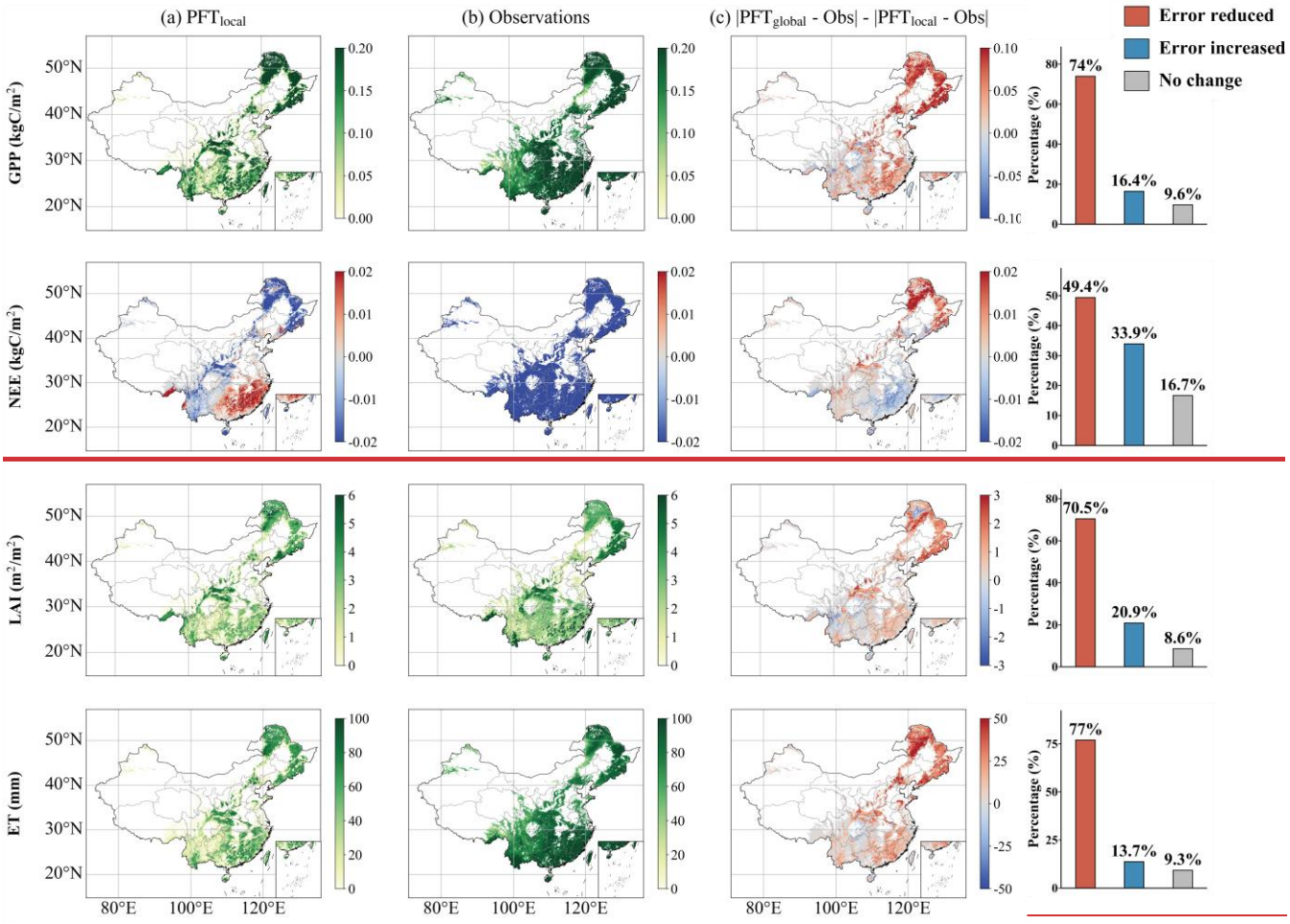
(a) PFT$_{local}$
(b) Observations
(c) |PFT$_{global}$ - Obs| - |PFT$_{local}$ - Obs|
Error reduced
Error increased
No change
GPP (kgC/m^2)
NEE (kgC/m^2)
LAI (m^2/m^2)
ET (mm)
Percentage (%)
74%
16.4%
9.6%
49.4%
33.9%
16.7%
70.5%
20.9%
8.6%
77%
13.7%
9.3%
50°N
40°N
30°N
20°N
80°E
100°E
120°E

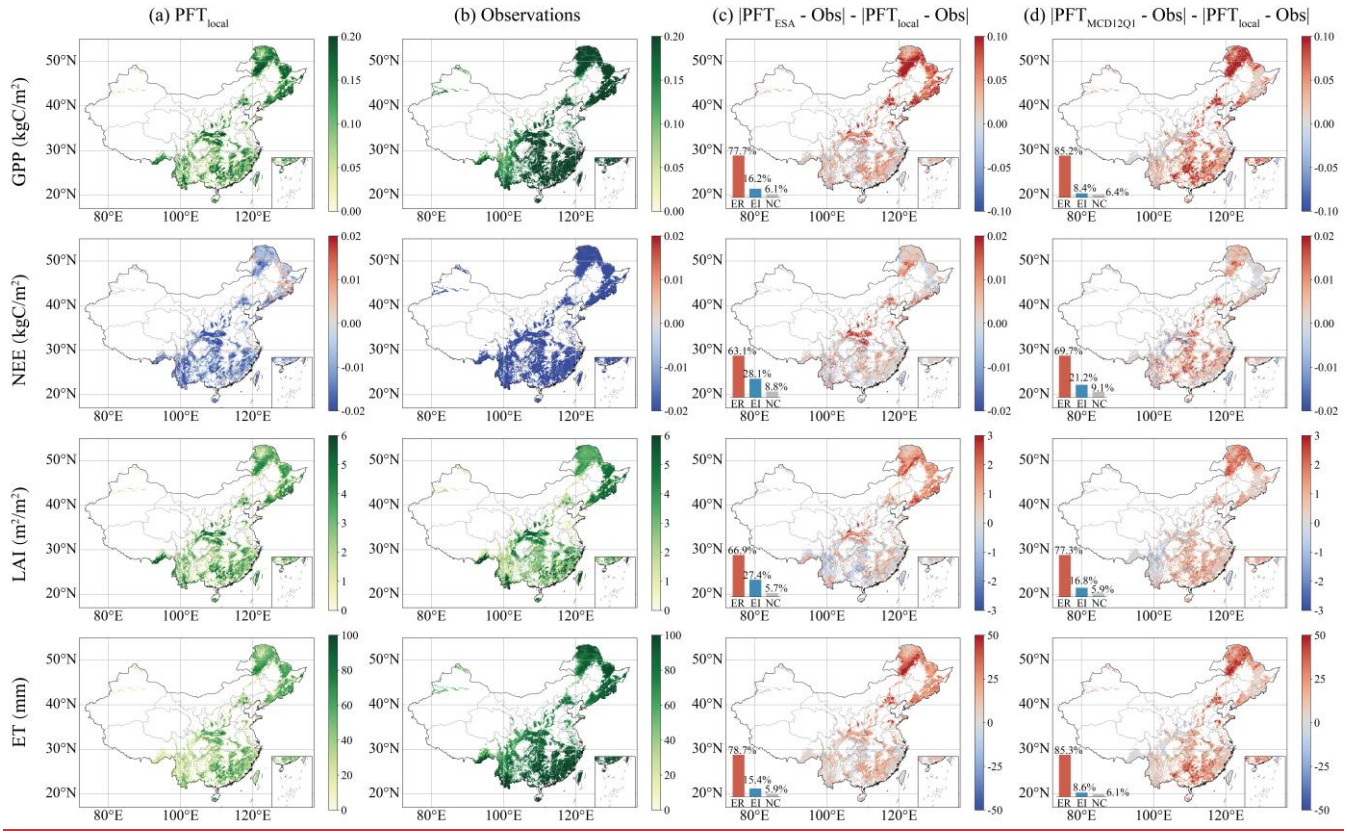

Figure ~~8~~9. Model-data comparison for gross primary productivity (GPP), net ecosystem exchange (NEE), leaf area index (LAI), and actual evapotranspiration (ET)~~GPP, NEE, LAI, and ET~~ for summer (June–August) 2010. **(a)** Ecosystem variables simulated by the Lund-Potsdam-Jena general ecosystem simulator (LPJ–GUESS) model using our reconstructed dataset ($\boldsymbol{PFT_{local}}$). **(b)** Corresponding observation-based benchmark products from FLUXCOM (GPP, NEE), GIMMS (LAI4g), and GLEAM (ET). **(c)** The difference in absolute error between model runs, quantifies the performance difference between our reconstructed dataset ($\boldsymbol{PFT_{local}}$) and the European Space Agency ($\boldsymbol{PFT_{ESA}}$) relative to the remote sensing observation products ($\boldsymbol{Obs}$), calculated as $|\boldsymbol{PFT_{ESAglobal}} - \boldsymbol{Obs}\sout{\boldsymbol{ervation}}| - |\boldsymbol{PFT_{local}} - \boldsymbol{Obs}\sout{\boldsymbol{ervation}}|$. **(d)** Same as **(c)**, but quantifying the performance difference against the MODIS land cover type product ($\boldsymbol{PFT_{MCD12Q1}}$), calculated as $|\boldsymbol{PFT_{MCD12Q1}} - \boldsymbol{Obs}| - |\boldsymbol{PFT_{local}} - \boldsymbol{Obs}|$. For both **(c)** and **(d)**, p~~P~~ositive values indicate that $\boldsymbol{PFT_{local}}$ reduces the simulation error (improves performance) compared to the global PFT datasets, whereas negative values indicate an increase in error (performance degradation), and the ~~right-hand~~ bar graph displays the percentages of error reduced (ER), increased (EI), and no change (NC).

High simulated GPP values (>0.2 kgC/m^2) are concentrated in the forested regions of northeastern (e.g., the Greater Khingan and Changbai Mountains), the central Qinling Mountains, and southeast China. Conversely, low GPP values are characteristic of the arid and semi-arid regions of the northwest and the Tibetan Plateau (Fig. ~~8a~~9a), where productivity is constrained by water availability and low temperatures. On a macroscale, the simulation accurately captures this geographical distribution. The PFT_{local} demonstrates a distinct advantage in terms of PFT forcing. Compared to $\boldsymbol{PFT_{ESA}}$, it reduces simulation errors across 77.7% of the domain (Fig. 9c), with improvements primarily concentrated in Northeast China, North China, and the Qinling Mountains (red areas); conversely, areas of increased error (16.2%) are sporadically distributed across southern China. The improvement is even more pronounced relative to $\boldsymbol{PFT_{MCD12Q1}}$, where error reductions cover 85.2% of the terrestrial area, while increased errors are confined to only 8.4% of the domain, specifically in Southwest China and Taiwan

(Fig. 9d). For NEE simulations, the PFT_{local} significantly outperforms $\boldsymbol{PFT_{ESA}}$, reducing errors across 63.1% of the domain (Fig. 9c). The most pronounced improvements are observed in the Qinling Mountains (indicated by deep red), while areas of increased error (28.1%, blue regions) are primarily concentrated in Northeast and Southwest China. Relative to $\boldsymbol{PFT_{MCD12Q1}}$, the extent of improvement expands to 69.7%, whereas error increases (21.2%) are mainly distributed across the Northeast, Southwest, and Taiwan regions (Fig. 9d).

~~However, the model tends to underestimate GPP compared to the FLUXCOM product, particularly in northern, central, and southwestern China (Fig. 8a and 8b). Regarding the impact of the PFT forcing, the map demonstrates a distinct advantage by reducing simulation errors across 74% of the domain, where it reduces simulation error (red areas in Fig. 8c). In other areas, such as southwestern and parts of central China, using increases the simulation error compared to (blue areas in Fig. 8c).~~

~~The simulation of NEE exhibits greater uncertainty compared to that of GPP. Observational data (Fig. 8b) indicate that China's forested regions function as strong carbon sinks during the summer (NEE < 0.02 kgC/m^2). While the driven simulation correctly identifies northeastern, central, and southwestern China as carbon sinks, it incorrectly depicts eastern China, particularly the southeast, as a strong carbon source (NEE > 0.02 kgC/m^2), thus failing to reproduce the observed magnitude of carbon uptake in these forests (Fig. 8a). Despite this systematic bias, the use of results in a substantial improvement of 49.4% in the simulation of NEE relative to (Fig. 8c). Across large portions of the country, especially in the northeast, the absolute error is substantially reduced (indicated by deep red coloration). The areas where simulation error increases (blue regions) are concentrated in parts of eastern and southeastern China.~~

~~The simulated LAI exhibits a spatial pattern analogous to that of GPP, characterized by a general decline in values from east to west. However, when compared against the observation-based data, the model demonstrates an underestimate of LAI, particularly pronounced in southern China. The application of the dataset substantially reduces LAI simulation errors across 70.5% of the domain (demarcated by red in Fig. 8c), underscoring the superiority of the new PFT map. Nevertheless, in some parts of the northeast and southwest, the LAI simulation error increases (blue areas), in strong spatial correspondence with the areas of increased GPP error.~~

Simulated LAI exhibits a spatial pattern analogous to that of GPP (Fig. 9a). Relative to $\boldsymbol{PFT_{ESA}}$, the PFT_{local} reduces errors across 66.9% of the domain (marked red in Fig. 9c), with the most pronounced improvements observed in the Northeast and Qinling regions; conversely, areas of increased error (27.4%, blue) are primarily situated in southern China. Compared to $\boldsymbol{PFT_{MCD12Q1}}$, the extent of error reduction expands to 77.3%, while increased errors (16.8%) are confined largely to Southwest China and Taiwan (Fig. 9d). Simulated ET exhibits a spatial pattern consistent with the other variables analysed (Fig. 9a). Regarding model improvement (Fig. 9c), the PFT_{local} reduces simulation errors across 78.7% of China relative to $\boldsymbol{PFT_{ESA}}$ (indicated by extensive red areas), except for certain parts of southern China. When compared against $\boldsymbol{PFT_{MCD12Q1}}$, this proportion rises to 85.3% (Fig. 9d). These results indicate that the reconstructed dataset demonstrates distinct superiority over the ESA and MCD12Q1 datasets in simulating major carbon and water fluxes across mainland China.

The simulation of ET demonstrates a spatial pattern consistent with the other variables analyzed. In simulations driven by , high ET values are concentrated in southeastern and northeastern China (Fig. 8a). Relative to remote sensing derived products (Fig. 8b), the model exhibits a general underestimation of ET. In terms of model improvement (Fig. 8c), substantially reduces the simulation error across 77% of China (indicated by large swaths of red), apart from some regions in the southwest.

5 Discussion

5.1 Comparison with other forest datasets

The spatial accuracy of the reconstructed PFT dataset was quantitatively evaluated against four existing products (MODIS, ESA CCI, CLCNMO, and GLC_FCS30). The assessment utilized 2,860 ground truth samples of needleleaf and broadleaf forests from nationwide field surveys conducted from 2011–2013 (Fig. S6). For direct comparison, all datasets were standardized to a 1km resolution within the same projection and spatial extent. The reconstructed PFT dataset achieved an overall classification accuracy of 88.51%, which is higher than MODIS (68.74%), ESA CCI (86.46%), CLCNMO (77.46%), and GLC_FCS30 (86.52%) (Table 5). Specifically: For broadleaf forests, the dataset's accuracy (89.12%) surpassed most products, though it was slightly lower than GLC_FCS30 (90.12%). For needleleaf forests, the dataset's accuracy (87.91%) was the highest among all evaluated products. Although the User's Accuracy (UA) and Producer's Accuracy (PA) were not uniformly superior, the dataset's F1 score (87.91%) was highest. This independent validation confirms the high spatial accuracy of the reconstructed PFT data in comparison to prominent existing datasets.

Table 5. Comparison of mapping accuracy based on ground-truth samples from 2011–2013 for this study, MODIS, ESA CCI, CLCNMO, and GLC_FCS30.

		Broadleaf				Needleleaf				Overall
		2011	2012	2013	Mean	2011	2012	2013	Mean	Mean
This study	PA (%)	82.35	86.79	93.92	87.69	77.52	84.81	81.38	81.24	84.46
	UA (%)	87.32	92.4	91.89	90.54	90.24	93.18	95.93	93.12	91.83
	F1 (%)	84.76	89.51	92.9	89.06	83.4	88.8	88.06	86.75	87.91
	OA (%)	85.41	89.93	92.02	89.12	84.35	89.19	90.18	87.91	88.51
MODIS	PA (%)	62.55	64.82	69.06	65.48	14.48	19.42	14.48	16.13	40.80
	UA (%)	90.37	92.68	88.65	90.57	96.2	92.45	91.3	93.32	91.94
	F1 (%)	73.93	76.29	77.64	75.95	25.17	32.1	25	27.42	51.69
	OA (%)	78.26	80.05	77.91	78.74	56.33	58.51	61.35	58.73	68.74
ESA_CCI	PA (%)	80	86.12	91.71	85.94	73.33	76.09	73.1	74.17	80.06
	UA (%)	89.28	92.21	91.21	90.90	91.02	92.75	92.98	92.25	91.58
	F1 (%)	84.38	89.06	91.46	88.30	81.22	83.6	81.85	82.22	85.26
	OA (%)	85.41	89.53	90.49	88.48	82.8	84.92	85.58	84.43	86.46
CLCNMO[a]	PA (%)	-	-	90.61	90.61	-	-	33.1	33.1	61.86

	UA (%)	-	-	83.25	83.25	-	-	100	100	91.63
	F1 (%)	-	-	86.77	86.77	-	-	49.74	49.74	68.26
	OA (%)	-	-	84.66	84.66	-	-	70.25	70.25	77.46
GLC_FCS30[b]	PA (%)	87.25	-	96.13	91.69	68.57	-	64.14	66.36	79.02
	UA (%)	88.65	-	90.16	89.41	95.49	-	97.89	96.69	93.05
	F1 (%)	87.94	-	93.05	90.50	79.82	-	77.5	78.66	84.58
	OA (%)	88.21	-	92.02	90.12	82.42	-	83.44	82.93	86.52

Notes: PA, UA and OA are abbreviations for the producer's accuracy, user's accuracy, and overall accuracy, respectively. The F1 represents the harmonic mean of the PA and the UA.

[a] The CLCNMO dataset was only available for 2013.

[b] The GLC_FCS30 dataset is produced at 5-year intervals. For this study's validation, its 2010 data was used as a proxy for 2011, and its 2015 data was used as a proxy for 2013.

The temporal evolution of the reconstructed PFT dataset aligns closely with NFI records, which document a significant increase in national forest cover from approximately 12% in the early 1980s to 24% at present, largely due to extensive afforestation programs (Fig. 5). In contrast, existing LULC products overwhelmingly fail to reproduce the historical trend of forest expansion in China since the 1980s (Fig. 5). Nearly all these datasets substantially underestimate the rate of forest growth. The CNLUCC dataset, for example, depicts a largely static forest area from 1980 to 2023, thereby failing to capture the marked gains resulting from China's afforestation programmes. Although the GLASS_GLC product indicates an increase, its forest area estimations are considerably higher than the official NFI statistics. Moreover, existing LULC products are unable to accurately resolve the divergent historical trajectories of needleleaf and broadleaf forests. Therefore, a re-evaluation of the impacts of China's forest cover change on terrestrial ecosystems using this newly developed, validated dataset is warranted.

5.2 A spatiotemporally constrained approach for reconstructing forest PFTs via multi-source data fusion

This study developed a method to integrate the "top-down" spatial detail derived from multi-source remote sensing products with the "bottom-up" statistical constraints provided by the NFI. The methodology involved harmonizing disparate LULC data sources into a uniform spatial framework via systematic resampling, re-projection, and aggregation. A consistency metric (CON) was computed to quantitatively assess spatial disagreements in forest identification among these sources. This metric functions as a diagnostic tool, elucidating inter-source congruence and leveraging this consensus to construct more robust maps of forest cover and PFTs; pixels with higher CON values are prioritized, whereas regions with low CON values, indicative of poor source data consensus, are assigned a lower priority unless their inclusion is mandated by NFI area constraints. This strategy effectively mitigates classification-level uncertainty by integrating a "majority vote" consensus with external statistical controls. Furthermore, the approach utilizes an annual maximum NDVI mask to delineate supplementary forest patches. This application of an NDVI mask, supported by prior research, effectively filters spurious forest signals from mountainous terrains, barren lands, and sparsely vegetated areas (Qin et al., 2015).This approach not only overcomes the limitations of relying on single data sources but also rectifies a well-documented defect in existing land cover products:

specifically, their frequent failure to adequately capture the extensive, policy-driven forest expansion trend in China since the 1980s, which leads to an underestimation of the forest cover growth rate (Fig. 5) (Yue et al., 2024; Zhu et al., 2025; Yu et al., 2022; Xia et al., 2023). Furthermore, existing LULC products lack the capability to accurately resolve the historical trajectories of needleleaf and broadleaf forest differentiation. Consequently, DGVMs driven by these historical datasets may severely underestimate China's carbon sink potential. We tested the hypothesis that a more accurate vegetation cover map improves land surface model performance by using our reconstructed PFT map to drive the LPJ–GUESS dynamic vegetation model. The results indicate that, compared to simulations using the ESA CCI and MODIS global PFT datasets, our dataset significantly improved the simulation accuracy of key ecosystem variables (Fig. 9). The spatial patterns of these improvements coincide highly with regions where the tree cover in our dataset differs most from global products, particularly in Northeast China (Figs. 7 and 8). This provides compelling evidence for the critical role of accurate vegetation representation in simulating carbon and water cycles. By providing a more precise depiction of historical forest dynamics, this dataset offers stronger constraints for the model parameterization of surface albedo, canopy structure, and transpiration, thereby enabling more robust flux estimates.

Notably, while both this study and Xia et al. (2023) aimed to reconstruct forest growth trends consistent with NFI records, certain discrepancies exist in the results. For instance, Xia et al. (2023) identified low forest classification consistency primarily in the northwestern regions of Xinjiang, Qinghai, and Ningxia, whereas our study observed low consistency solely in Ningxia. This divergence likely stems from our adoption of a stricter NFI area constraint—specifically, utilising 'wooded land' (excluding shrubland) rather than total forest area. By excluding shrublands, our extracted distribution of 'potential forest' aligns more closely with the actual forest distribution in sparsely forested regions such as Xinjiang and Qinghai. Furthermore, a comparison of data between 1990 and 1995 by Xia et al. (2023) suggested a relatively low area of forest loss in China during this period. In contrast, our dataset reveals the opposite trend, identifying a peak in forest loss between 1991 and 1994. This difference is likely attributable to the annual temporal resolution of our dataset, which offers heightened sensitivity to forest gain and loss events. Finally, our dataset provides a comprehensive annual time series of nine distinct forest PFTs spanning the period 1981–2023. It is therefore necessary to utilize this newly developed and validated dataset to systematically re-evaluate the impacts of forest cover change on terrestrial ecosystems in China.

~~Therefore, our methodology addresses the intrinsic limitations of relying on a single data modality, resolving a well-documented deficiency in extant land cover products. Specifically, these products often fail to represent the full extent of the significant, policy-driven expansion of Chinese forests post-1980, thereby underestimating the rate of forest cover growth (Fig. 5) (Yue et al., 2024; Zhu et al., 2025; Yu et al., 2022). Consequently, DGVMs driven by these historically inaccurate datasets are likely to substantially underestimate China's carbon sink. We tested the hypothesis that a more accurate vegetation map would improve land surface model performance. Driving the LPJ–GUESS dynamic vegetation model with our reconstructed PFT maps resulted in markedly improved simulations compared to those using the ESA CCI global PFT dataset (Fig. 8 and Fig. S10). The spatial pattern of these improvements aligns directly with regions where our dataset's tree cover diverges most from the global product, especially in northeastern China (Fig. 7 and Fig. S9). This provides powerful evidence for the critical role of accurate vegetation representation in simulating carbon and water cycles. By providing a more precise depiction of~~

~~historical forest dynamics, our dataset offers stronger constraints on model parameterizations of surface albedo, canopy structure, and transpiration, leading to more robust flux estimations.~~

~~5.3 Limitations and future work~~

However, this study is subject to certain uncertainties and limitations that need to be addressed in future work. First, as an integrated data product, our dataset inherits uncertainties from its primary sources: the input LULC data and the NFI statistics. Most satellite--based LULC datasets rely on machine learning classifiers, whose accuracy is contingent upon the representativeness, quantity, and quality of training samples. Furthermore, our dataset's accuracy is substantially dependent on the NFI data, which possesses its own uncertainties stemming from inventory methodologies and the representativeness of ground plots. Notably, the precision of NFI data has improved over time due to the progressive evolution of its sampling design; for example, the introduction of combined ground-truth and remote sensing samples in the fourth NFI (1989–1993) and a significant increase in remote sensing samples since the sixth NFI (1999–2003) markedly enhanced its accuracy (Lei et al., 2009). Consequently, any uncertainty within the NFI data will inevitably propagate into our reconstructed dataset.

~~Second, for provinces with limited historical data (e.g., Chongqing, Hong Kong, and Macau), we employed linear extrapolation to generate annual provincial-level statistics. This approach was predicated on prior findings that national afforestation targets exhibit a quasi-linear temporal trend (an increase of ~1.8 million ha/year) (He et al., 2024; Xu et al., 2023), suggesting a consistent, progressive afforestation strategy driven by government policy. Nevertheless, this method introduces a degree of uncertainty (Fig. S1). To mitigate this, we constrained the extrapolated area by defining a consistency level threshold, which was selected to ensure that the cumulative area of all pixels at or above this level most closely matched the target value for a given year. While this technique maximizes spatial and quantitative accuracy under the available data constraints, discrepancies may still exist between our reconstructed results and the actual forest area in these provinces prior to 2003, where the true conditions are unknown.~~

Secondly, this study employs consistency maps, derived from the aggregation of multi-source data spanning 1981–2023, to guide the annual classification of PFTs (see Sect. 3.4.1). This approach is predicated on the core assumption that the spatial distribution patterns of PFTs (e.g., needleleaf versus broadleaf forests) remained relatively stable throughout the study period. This assumption is considered reasonable at our 1 km study scale for several reasons: First, the biogeographical distribution of needleleaf and broadleaf forests is primarily governed by long-term, relatively stable climatic, edaphic, and topographic conditions (Fragnière et al., 2015; Steidinger et al., 2019). For instance, broadleaf forests typically require longer growing seasons and warmer temperatures, whereas needleleaf forests exhibit greater tolerance to low temperatures and shorter growing seasons. These distinct ecological niches imply that large-scale transitions between these forest types are unlikely to occur in the absence of significant climate change or extensive, sustained anthropogenic intervention. Our analysis based on GLC_FCS30D (30 m), ESA CCI (300 m), and MCD12Q1 (500 m) data indicates that mutual transitions between needleleaf and broadleaf forests over five-year intervals account for only 0%–0.34% of the total area of these types in the end year (Table S4); such minor fluctuations are virtually negligible when upscaled to a 1 km resolution. Nevertheless, this study acknowledges

its inability to capture PFT transitions induced by short-term, fine-scale disturbances (e.g., tree species replacement following logging). Given the high spectral similarity between needleleaf and broadleaf forests, accurately monitoring dynamic changes between different PFTs at the national scale using historical imagery (e.g., Landsat) was extremely challenging prior to the availability of high-resolution data in 2015 (e.g., 10 m Sentinel-2 data) (Klehr et al., 2025). The primary objective of this research is to provide a long-term PFT time series dataset that is consistent with historical NFI data. Future work could leverage advanced machine learning methodologies, such as 3D-CNNs (Mäyrä et al., 2021) and regression-based unmixing (Klehr et al., 2025), to fully exploit temporal phenological features and multi-scale textural information from satellite imagery. These approaches would enhance the differentiation of canopy structures and seasonal phenology between needleleaf and broadleaf forests, thereby further improving the capability to detect PFT change events.

~~Finally, while our PFT distribution map significantly improves the simulation performance of DGVMs compared to the ESA CCI PFT product, this model-based validation is relative, not absolute. This can lead to discrepancies between simulated outcomes and on the ground reality (Fig. 8a, b, Fig. S10a, b), with errors potentially attributable to the internal parameterization of the LPJ–GUESS model. The model's default parameters are primarily calibrated for European ecosystems and may not align with the unique ecophysiology, disturbance regimes, and soil hydrology of China (Li et al., 2022; Peng et al., 2019). A comprehensive, large-scale parameter calibration for China was beyond the scope of this study. A key avenue for future research is to disentangle the interacting uncertainties among data inputs, model structure, and climate drivers. Enhancing differentiated, regional-scale modeling and identifying underlying mechanisms will be critical for improving the predictive power of terrestrial ecosystem models and the accuracy of forest carbon sink estimations in China.~~

Finally, while our PFT distribution map significantly enhances the simulation accuracy of DGVMs compared to the ESA CCI and MCD12Q1 PFT products, this model-based validation is relative, not absolute. This can lead to discrepancies between simulated outcomes and on-the-ground reality (see Fig. 9a, b), with residual errors potentially attributable to the LPJ–GUESS model structure. The model was primarily developed for European ecosystems (Meyer et al., 2025; Gregor et al., 2024), and may not align with China's unique ecophysiological characteristics, disturbance regimes, and soil hydrological conditions (Li et al., 2022; Peng et al., 2019b). While this study performed only preliminary calibration of PFT ecophysiological parameters (Table S3), the model's behaviour is governed not by a single PFT process, but by the complex interplay of photosynthetic efficiency, carbon allocation strategies, and biomass turnover rates. Crucially, the importance of these processes varies significantly across environmental gradients: for instance, in humid, high-productivity forest ecosystems, the system operates closer to its maximum photosynthetic potential. In such complex and layered canopies, parameters associated with regeneration and light competition (shade_tolerant, est_max) become paramount. Conversely, in water-limited arid and semi-arid ecosystems, control significantly shifts to parameters governing resource acquisition and allocation. Here, the primary challenge is survival under stress, not maximizing production. Consequently, GM (stomatal conductance) and reprfrac (allocation) become exceptionally important, reflecting the different limiting factors shaping real-world ecosystems. Given China's vast and geographically diverse territory, encompassing arid, semi-arid, semi-humid, and humid ecosystems, this study did not include comprehensive, large-scale parameter calibration. The key direction for future research is to disentangle the

interacting uncertainties among data inputs, model structure, and climate drivers. Enhancing differentiated regional-scale modelling and revealing underlying mechanisms will be critical for improving the predictive power of terrestrial ecosystem models and the accuracy of forest carbon sink estimation in China.

6 Data availability

The reconstructed forest cover dataset generated in this study is publicly available in the Zenodo repository at https://doi.org/10.5281/zenodo.17656153~~10.5281/zenodo.16208012~~ (Liu et al., 2025). All third-party datasets used for this analysis are publicly available from their original sources as listed below: National Forest Inventory records for China are accessible from the National Forestry and Grassland Data Center at http://www.forestdata.cn/. The following datasets are available from the Resource and Environment Science and Data Center (https://www.resdc.cn/): the China National Land Use/Cover Change (CNLUCC), Moderate Resolution Land Use and Cover (MLUD), and Wu_LC datasets (last access: 7 May 2025). The following datasets were accessed via Google Earth Engine (https://code.earthengine.google.com): the Copernicus Global Land Service (CGLS), MODIS Land Cover Type (MCD12Q1), Hansen Global Forest Change (Hansen), JRC Forest Types, and Global Forest Canopy Height (GFCH) (last access: 13 April 2025). The following datasets are provided by the European Space Agency (ESA) (http://climate.esa.int/en/projects/land-cover): ESACCI_LC, GlobCover, and ESA_WorldCover (last access: 12 April 2025). FROM_GLC is accessible from Tsinghua University's data portal (http://data.ess.tsinghua.edu.cn) (last access: 10 April 2025).~~Datasets from Tsinghua University (http://data.ess.tsinghua.edu.cn), including FROM_GLC, GLASS_GLC, and the first all-season sample set for mapping global land cover with Landsat 8 data, were accessed from their data portal (last access: 10 April 2025).~~ The China Land Cover Dataset (CLCD) is publicly available at https://doi.org/10.5281/zenodo.4417810 (Yang and Huang, 2021). The Global Land-Cover-Related Datasets with Fine Classification System (GLC_FCS30D) is publicly available at https://doi.org/10.5281/zenodo.8239305 (Liu et al., 2023). Global Forest Cover 30m (GFC30) is available from the Data Sharing and Service Portal at https://data.casearth.cn/dataset/6188d5be819aec0dc5853a4d (last access: 10 April 2025). Global Land Cover 2000 (GLC2000) is available from the National Earth System Science Data Center at https://www.geodata.cn/data/datadetails.html?dataguid=60781990406898&docId=12324 (last access: 10 April 2025). Consensus Land Cover of northern mid-to-high latitudes (G~~C~~LCNMO) is publicly available at https://globalmaps.github.io/glcnmo.html (last access: 12 April 2025). GlobeLand30 is available for download from the National Geomatics Center of China at http://www.globallandcover.com/ (last access: 10 April 2025). Land cover map of China in 2000 is available from the National Tibetan Plateau Data Center at https://doi.org/10.11888/Socioeco.tpdc.270467 (last access: 11 October 2025) (Ran et al., 2009). The 1 km monthly mean temperature dataset for China is available from the National Tibetan Plateau Data Center at https://doi.org/10.11888/Meteoro.tpdc.270961 (last access: 27 October 2025) (Peng et al., 2019a). China meteorological forcing data (CMFD 2.0) are publicly available from the National Tibetan Plateau Data Center at https://doi.org/10.11888/Atmos.tpdc.302088 (last access: 24 September 2025) (He et al., 2020). China dataset of soil

properties for land surface modelling version 2 (CSDL v2) (Shi et al., 2025) is publicly available at https://www.scidb.cn/s/ZZJzAz (last access: 23 September 2025). China's first seamless annual leaf-on (growing season) Landsat composite dataset (1985–2023) is available on the GEE platform (https://ee-caiyt33-catcd.projects.earthengine.app/view/landsat-yearly-composite-viewer, last access: 20 October 2025) (Cai et al., 2025). Treecover2010 (TCC) data are freely available from the University of Maryland at https://glad.umd.edu/Potapov/TCC_2010/. ~~Long-term Normalized Difference Vegetation Index (Jeong's NDVI) is available from Seoul National University at https://www.environment.snu.ac.kr/data/long-term-vi (last access: 11 April 2025).~~ The Köppen–Geiger climate classification maps are available from Figshare at https://figshare.com/articles/dataset/Present_and_future_K_ppen-Geiger_climate_classification_maps_at_1-km_resolution/6396959/2 (last access: 26 May 2025). A global topographic dataset is publicly available from Earthenv at https://www.earthenv.org/topography (last access: 25 May 2025). ~~ERA5-Land monthly averaged data (2m temperature, total precipitation, surface solar radiation downwards) are publicly available from the Copernicus Climate Data Store at https://cds.climate.copernicus.eu/datasets/reanalysis-era5-land-monthly-means?tab=overview (last access: 21 September 2024).~~ Fluxcom GPP and NEE products are available from the project website at https://fluxcom.org/CF-Products/ (last access: 10 January 2025). GIMMS LAI4g is publicly available in the Zenodo repository at https://doi.org/10.5281/zenodo.7649107 (Cao et al., 2023). GLEAM Evapotranspiration (ET) products are available for download at https://www.gleam.eu/#downloads (last access: 23 July 2024).

7 Conclusion

To address the failure of existing land cover products in capturing the extensive forest expansion from large-scale afforestation in China since ~~1980~~1981, this study presents a reconstructed dataset of annual forest cover at 1 km resolution for the period ~~1980~~1981–2023 and the distribution of ~~eight~~ nine PFTs ~~from 1981–2013~~. This paper details a method that integrates spatial forest distribution constraints from a suite of remote sensing products with provincial-level forest area constraints from the NFI. The resultant dataset reproduces NFI-consistent forest dynamics ($R^2 \approx 1$) with an ~~95.3~~84.86% overall accuracy ~~(≈ 1)~~. When applied within a DGVM, the simulation accuracy of key ecosystem variables is improved across 63.1%–85.3% of China's terrestrial area compared to the ESA CCI and MCD12Q1 datasets. ~~and its application within a DGVM markedly improves the simulation accuracy of key ecosystem variables by 49.4% to 77%.~~ This work thus provides a critical data foundation for more robust assessments of the ecological effects of forest restoration and for refining regional carbon sink estimations. ~~The dataset's reliability is, however~~However, the dataset's reliability is inherently constrained by uncertainties in the methodology and source data, making it difficult to detect PFT transitions induced by short-term, small-scale, or abrupt events. Furthermore, future research should aim to decouple the interplay between data inputs, model structure, and climate drivers to advance the predictive capability of ecosystem models further. ~~inherently constrained by uncertainties in the source data, particularly in highly fragmented landscapes. Future research should therefore aim to decouple the interplay between data inputs, model structure, and climate drivers to advance the predictive capability of ecosystem models further.~~

Author contributions

Conceptualization, Bo.L., Boy.L., J.L., and Q.F.; Data curation, Bo.L.; Formal analysis, Bo.L.; Investigation, Bo.L., F.F., and Y.B.; Methodology, Bo.L.; Supervision, Boy.L., J.L., and Q.F.; Validation, Bo.L., F.F., and Y.B.; Visualization, Bo.L. and Y.B.; Writing (original draft preparation), Bo.L.; Writing (review and editing), Boy.L. All authors have read and agreed to the published version of the manuscript.

Competing interests

The authors declare that they have no conflict of interest.

Acknowledgements

The authors greatly appreciate the numerous organizations that made their data publicly available for this research. We sincerely thank the ESA for providing the ESACCI_LC, GlobCover, and ESA_WorldCover products; the Copernicus Programme for the CGLS dataset; and the National Aeronautics and Space Administration (NASA) for the MCD12Q1 product. We acknowledge the data providers in China, including: the National Forestry and Grassland Data Center for the national forest inventory records; the Resource and Environment Science and Data Center (RESDC) for the CNLUCC, MLUD, and Wu_LC datasets; the National Geomatics Center of China for the GlobeLand30 dataset; the Data Sharing and Service Portal for the GFC30 dataset; the National Earth System Science Data Center for the GLC2000 dataset; and the National Tibetan Plateau Data Center (TPDC) for providing the land cover map of China in 2000, the 1 km monthly mean temperature dataset, and the CMFD 2.0. We also extend special thanks to Tsinghua University for providing the FROM_GLC; and to the research teams who developed and openly shared the CLCD, GLC_FCS30D, GLCNMO, CSDL v2, and the seamless annual Landsat composite datasets. We also extend our thanks to the University of Maryland for the Hansen Global Forest Change dataset and TCC datasets; the Joint Research Centre of the European Commission for the JRC Forest Types dataset; the Earthenv repository for the global topographic dataset; and the providers of the FLUXCOM, GIMMS and GLEAM products. Finally, we offer our sincere gratitude to the developers of the LPJ–GUESS model for providing a valuable simulation tool, and to the Google Earth Engine team for developing and maintaining their powerful, planetary-scale platform for geospatial analysis. We also wish to acknowledge the AI model, Gemini 2.5 Pro, for its assistance in improving the language and style of the manuscript and in editing and inserting references.

~~The authors greatly appreciate the numerous organizations that made their data publicly available for this research. We sincerely thank the ESA for providing the ESACCI_LC, GlobCover, and ESA_WorldCover products; and the National Aeronautics and Space Administration (NASA) for the MCD12Q1 product. We acknowledge the data providers in China, including: the National Forestry and Grassland Data Center for the national forest inventory records; the Resource and Environment Science and Data Center (RESDC) for the CNLUCC, MLUD, and Wu_LC datasets; the National Geomatics~~

~~Center of China for the GlobeLand30 dataset; the Data Sharing and Service Portal for the GFC30 dataset; and the National Earth System Science Data Center for the GLC2000 dataset. We also extend special thanks to Tsinghua University for providing the FROM_GLC and GLASS_GLC datasets, as well as the first all-season sample set for mapping global land cover with Landsat-8 data. We also extend our thanks to the University of Maryland for the Hansen Global Forest Change dataset; the Joint Research Centre of the European Commission for the JRC Forest Types dataset; Seoul National University for the Jeong's NDVI data; the Copernicus Climate Data Store for the ERA5-Land reanalysis data; the Earthenv repository for the global topographic dataset; and the providers of the FLUXCOM, GIMMS and GLEAM products. Finally, we offer our sincere gratitude to the developers of the LPJ-GUESS model for providing a valuable simulation tool, and to the Google Earth Engine team for developing and maintaining their powerful, planetary-scale platform for geospatial analysis. We also wish to acknowledge the AI model, Gemini 2.5 Pro, for its assistance in improving the language and style of the manuscript and in editing and inserting references.~~

Financial support

This research was supported by the National Natural Science Foundation of China (grant no. 42371101), the Young Science and Technology New Star Project of Shaanxi Province (grant no. 2024ZC-KJXX-013), the Qin Chuangyuan Cites High-level Innovation or Entrepreneurship Talent Project (grant no. QCYRCXM-2023-066), the fifth batch special funding (Pre-Station) from China Postdoctoral Science Foundation (grant no. 2023TQ0207), and the Fundamental Research Funds for the Central Universities (grant nos. GK202304024, 1110011297, 1112010355).

References

Alkama, R., and Cescatti, A.: Biophysical climate impacts of recent changes in global forest cover, *Science*, 351, 600–604, https://doi.org/10.1126/science.aac8083, 2016.

Amatulli, G., Domisch, S., Tuanmu, M.-N., Parmentier, B., Ranipeta, A., Malczyk, J., and Jetz, W.: A suite of global, cross-scale topographic variables for environmental and biodiversity modelling, *Sci. Data*, 5, 1–15, https://doi.org/10.1038/sdata.2018.40, 2018.

Beck, H. E., Zimmermann, N. E., McVicar, T. R., Vergopolan, N., Berg, A., and Wood, E. F.: Present and future Köppen-Geiger climate classification maps at 1-km resolution, *Sci. Data*, 5, 1–12, https://doi.org/10.1038/sdata.2018.214, 2018.

Bergkvist, J., Lagergren, F., Islam, M. R., Wårlind, D., Miller, P. A., Finnander Linderson, M. L., Lindeskog, M., and Jönsson, A. M.: Quantifying the impact of climate change and forest management on Swedish forest ecosystems using the dynamic vegetation model LPJ-GUESS, *Earth's Future*, 13, e2024EF004662, https://doi.org/10.1029/2024EF004662, 2025.

Bonan, G. B., Levis, S., Kergoat, L., and Oleson, K. W.: Landscapes as patches of plant functional types: An integrating concept for climate and ecosystem models, *Global Biogeochem. Cy.*, 16, 5-1, https://doi.org/10.1029/2000GB001359, 2002.

Cai, Y., Li, X., Zhu, P., Nie, S., Wang, C., Liu, X., and Chen, Y.: China Earth Observation Data Cube: The 30-m Seamless Annual Leaf-On Landsat Composites from 1985 to 2023, *J. Remote Sens.*, 5, 0698, https://doi.org/10.34133/remotesensing.0698, 2025.

Cao, S., Li, M., Zhu, Z., Wang, Z., Zha, J., Zhao, W., Duanmu, Z., Chen, J., Zheng, Y., Chen, Y., Myneni, R. B., and Piao, S.: Spatiotemporally consistent global dataset of the GIMMS Leaf Area Index (GIMMS LAI4g) from 1982 to 2020 (V1.2). Zenodo [data], https://doi.org/10.5281/zenodo.7649107, 2023.

Chen, C., Park, T., Wang, X., Piao, S., Xu, B., Chaturvedi, R. K., Fuchs, R., Brovkin, V., Ciais, P., and Fensholt, R.: China and India lead in greening of the world through land-use management, *Nat. Sustain.*, 2, 122–129, https://doi.org/10.1038/s41893-019-0220-7, 2019.

Chen, H., Zhu, Q., Peng, C., Wu, N., Wang, Y., Fang, X., Gao, Y., Zhu, D., Yang, G., and Tian, J.: The impacts of climate change and human activities on biogeochemical cycles on the Qinghai-Tibetan Plateau, *Glob. Change Biol.*, 19, 2940–2955, https://doi.org/10.1111/gcb.12277, 2013.

Chen, J., Chen, J., Liao, A., Cao, X., Chen, L., Chen, X., He, C., Han, G., Peng, S., and Lu, M.: Global land cover mapping at 30 m resolution: A POK-based operational approach, *ISPRS J. Photogramm. Remote Sens.*, 103, 7–27, https://doi.org/10.1016/j.isprsjprs.2014.09.002, 2015.

Cheng, K., Chen, Y., Xiang, T., Yang, H., Liu, W., Ren, Y., Guan, H., Hu, T., Ma, Q., and Guo, Q.: 2020 forest age map for China with 30 m resolution, *Earth Syst. Sci. Data*, 16, 803-819, https://doi.org/10.5194/essd-16-803-2024, 2024.

Chini, L., Hurtt, G., Sahajpal, R., Frolking, S., Klein Goldewijk, K., Sitch, S., Ganzenmüller, R., Ma, L., Ott, L., and Pongratz, J.: Land-use harmonization datasets for annual global carbon budgets, *Earth Syst. Sci. Data*, 13, 4175–4189, https://doi.org/10.5194/essd-13-4175-2021, 2021.

Fang, J., Chen, A., Peng, C., Zhao, S., and Ci, L.: Changes in forest biomass carbon storage in China between 1949 and 1998, *Science*, 292, 2320–2322, https://doi.org/10.1126/science.1058629, 2001.

Fang, X., Zhao, W., Zhang, C., Zhang, D., Wei, X., Qiu, W., and Ye, Y.: Methodology for credibility assessment of historical global LUCC datasets, *Sci. China Earth Sci.*, 63, 1013–1025, https://doi.org/10.1007/s11430-019-9592-y, 2020.

Food and Agriculture Organization of the United Nations. State of the world's forests 2016. Forests and agriculture: Land-use challenges and opportunities. FAO Report, 2016.

Fragnière, Y., Bétrisey, S., Cardinaux, L., Stoffel, M., and Kozlowski, G. J. J.: Fighting their last stand? A global analysis of the distribution and conservation status of gymnosperms, *J. Biogeogr.*, 42, 809–820, https://doi.org/10.1111/jbi.12480, 2015.

Friedlingstein, P., O'Sullivan, M., Jones, M. W., Andrew, R. M., Hauck, J., Landschützer, P., Le Quéré, C., Li, H., Luijkx, I. T., and Olsen, A.: Global carbon budget 2024, *Earth Syst. Sci. Data*, 17, 965–1039, https://doi.org/10.5194/essd-2024-519, 2025.

García, M. L., and Caselles, V.: Mapping burns and natural reforestation using Thematic Mapper data, *Geocarto Int.*, 6, 31–37, https://doi.org/10.1080/10106049109354290, 1991.

Ge, Q., Dai, J., He, F., Pan, Y., and Wang, M.: Land use changes and their relations with carbon cycles over the past 300 a in China, *Sci. China Ser. D Earth Sci.*, 51, 871–884, https://doi.org/10.1007/s11430-008-0067-8, 2008.

Gregor, K., Reyer, C. P., Nagel, T. A., Mäkelä, A., Krause, A., Knoke, T., and Rammig, A.: Reconciling the EU forest, biodiversity, and climate strategies, *Global Change Biol.*, 30, e17431, https://doi.org/10.1111/gcb.17431, 2024.

Hansen, M. C., Potapov, P. V., Moore, R., Hancher, M., Turubanova, S. A., Tyukavina, A., Thau, D., Stehman, S. V., Goetz, S. J., and Loveland, T. R.: High-resolution global maps of 21st-century forest cover change, *Science*, 342, 850–853, https://doi.org/10.1126/science.1244693, 2013.

Harper, K. L., Lamarche, C., Hartley, A., Peylin, P., Ottlé, C., Bastrikov, V., San Martín, R., Bohnenstengel, S. I., Kirches, G., and Boettcher, M.: A 29-year time series of annual 300 m resolution plant-functional-type maps for climate models, *Earth Syst. Sci. Data*, 15, 1465–1499, https://doi.org/10.5194/essd-15-1465-2023, 2023.

Hartung, K., Bastos, A., Chini, L., Ganzenmüller, R., Havermann, F., Hurtt, G. C., Loughran, T., Nabel, J. E. M. S., Nützel, T., and Obermeier, W. A.: Bookkeeping estimates of the net land-use change flux–a sensitivity study with the CMIP6 land-use dataset, *Earth Syst. Sci. Data*, 12, 763–782, https://doi.org/10.5194/essd-12-763-2021, 2021.

He, J., Yang, K., Tang, W., Lu, H., Qin, J., Chen, Y. Y., and Li, X.: The first high-resolution meteorological forcing dataset for land process studies over China, *Sci. Data*, 7, 25, https://doi.org/10.1038/s41597-020-0369-y, 2020.

He, Y., Piao, S., Ciais, P., Xu, H., and Gasser, T.: Future land carbon removals in China consistent with national inventory, *Nat. Commun.*, 15, 10426, https://doi.org/10.1038/s41467-024-54846-2, 2024.

Hong, S., Yin, G., Piao, S., Dybzinski, R., Cong, N., Li, X., Wang, K., Peñuelas, J., Zeng, H., and Chen, A.: Divergent responses of soil organic carbon to afforestation, *Natl. Sci. Rev.*, 3, 694–700, https://doi.org/10.1093/nsr/nwz203, 2020.

Houghton, R. A., and Hackler, J. L.: Sources and sinks of carbon from land-use change in China, *Global Biogeochem. Cy.*, 17, 1034, https://doi.org/10.1029/2002GB001970, 2003.

Industry Development Sub-center, Statistical Table of Main Indicators of Forest Resources by Province (Autonomous Region, Municipality) in the Ninth National Class I Forest Inventory, National Forestry and Grassland Scientific Data Center, 2018, CSTR:17575.11.0120230320014.0018.V1.

Islam, M. R., Jönsson, A. M., Bergkvist, J., Lagergren, F., Lindeskog, M., Mölder, M., Scholze, M., and Kljun, N.: Projected effects of climate change and forest management on carbon fluxes and biomass of a boreal forest, *Agric. For. Meteorol.*, 349, 109959, https://doi.org/10.1016/j.agrformet.2024.109959, 2024.

~~Jeong, S., Ryu, Y., Gentine, P., Lian, X., Fang, J., Li, X., Dechant, B., Kong, J., Choi, W., and Jiang, C.: Persistent global greening over the last four decades using novel long-term vegetation index data with enhanced temporal consistency, *Remote Sens. Environ.*, 311, 114282, https://doi.org/10.1016/j.rse.2024.114282, 2024.~~

Kennedy, R. E., Yang, Z., and Cohen, W. B.: Detecting trends in forest disturbance and recovery using yearly Landsat time series: 1. LandTrendr – temporal segmentation algorithms, *Remote Sens. Environ.*, 114, 2897–2910, https://doi.org/10.1016/j.rse.2010.07.008, 2010.

Kennedy, R. E., Yang, Z., Gorelick, N., Braaten, J., Cavalcante, L., Cohen, W. B., and Healey, S.: Implementation of the LandTrendr algorithm on Google Earth Engine, *Remote Sens.*, 10, 691, https://doi.org/10.3390/rs10050691, 2018.

Klehr, D., Stoffels, J., Hill, A., Pham, V.-D., van der Linden, S., and Frantz, D.: Mapping tree species fractions in temperate mixed forests using Sentinel-2 time series and synthetically mixed training data, *Remote Sens. Environ.*, 323, 114740, https://doi.org/10.1016/j.rse.2025.114740, 2025.

Lamarque, J.-F., Dentener, F., McConnell, J., Ro, C.-U., Shaw, M., Vet, R., Bergmann, D., Cameron-Smith, P., Dalsoren, S., and Doherty, R.: Multi-model mean nitrogen and sulfur deposition from the Atmospheric Chemistry and Climate Model Intercomparison Project (ACCMIP): evaluation of historical and projected future changes, *Atmos. Chem. Phys.*, 13, 7997–8018, https://doi.org/10.5194/acp-13-7997-2013, 2013.

Lei, X., Tang, M., Lu, Y., Hong, L., and Tian, D.: Forest inventory in China: status and challenges, *Int. Forest. Rev.*, 11, 52–63, https://doi.org/10.1505/ifor.11.1.52, 2009.

~~Li, C., Gong, P., Wang, J., Zhu, Z., Biging, G. S., Yuan, C., Hu, T., Zhang, H., Wang, Q., and Li, X.: The first all-season sample set for mapping global land cover with Landsat-8 data, *Sci. Bull.*, 62, 508–515, https://doi.org/10.1016/j.scib.2017.03.011, 2017.~~

Li, X., Zhang, H., Shang, R., Chen, J., Wang, D., Zhu, J., Huang, H., Lin, S., Pan, B., and Yuan, W.: It is time to optimize forest management policy for both carbon sinks and wood harvest in China, *Natl. Sci. Rev.*, 12, nwae464, https://doi.org/10.1093/nsr/nwae464, 2025.

Li, Y., Wang, Y., Sun, Y., and Li, J.: Global sensitivity analysis of the LPJ model for *L~~l~~arix olgensis* Henry forests NPP in Jilin Province, China, *Forests*, 13, 874, https://doi.org/10.3390/f13060874, 2022.

Lindeskog, M., Lagergren, F., Smith, B., and Rammig, A.: Accounting for forest management in the estimation of forest carbon balance using the dynamic vegetation model LPJ-GUESS (v4. 0, r9333): Implementation and evaluation of simulations for Europe, *Geosci. Model Dev.*, 14, 5887–5925, https://doi.org/10.5194/gmd-14-5887-2021, 2021.

Liu, B., Li, B., Feng, F., Bao, Y., Li, J., and Feng, Q.: 1 km annual forest cover and plant functional types dataset for China from ~~1980~~ 1981 to 2023. Zenodo [data], https://doi.org/10.5281/zenodo.17656153~~https://doi.org/10.5281/zenodo.16208012~~, 2025.

Liu, J., Li, S., Ouyang, Z., Tam, C., and Chen, X.: Ecological and socioeconomic effects of China's policies for ecosystem services, *Proc. Natl. Acad. Sci. U.S.A.*, 105, 9477–9482, https://doi.org/10.1073/pnas.0706436105, 2008.

Liu, L., Zhang, X., and Zhao T.: GLC_FCS30D: the first global 30-m land-cover dynamic monitoring product with fine classification system from 1985 to 2022, Zenodo [data], https://doi.org/10.5281/zenodo.8239305, 2023.

Liu, S., Bond-Lamberty, B., Boysen, L. R., Ford, J. D., Fox, A., Gallo, K., Hatfield, J., Henebry, G. M., Huntington, T. G., and Liu, Z.: Grand challenges in understanding the interplay of climate and land changes, *Environ. Int.*, 21, 1–43, https://doi.org/10.1016/j.envint.2016.09.007, 2017.

Mäyrä, J., Keski-Saari, S., Kivinen, S., Tanhuanpää, T., Hurskainen, P., Kullberg, P., Poikolainen, L., Viinikka, A., Tuominen, S., and Kumpula, T.: Tree species classification from airborne hyperspectral and LiDAR data using 3D convolutional neural networks, *Remote Sens. Environ.*, 256, 112322, https://doi.org/10.1016/j.rse.2021.112322, 2021.

Meyer, B. F., Darela-Filho, J. P., Gregor, K., Buras, A., Gu, Q. L., Krause, A., Liu, D., Papastefanou, P., Asuk, S., Grams, T. E. E., Zang, C. S., and Rammig, A.: Simulating the drought response of European tree species with the dynamic vegetation model LPJ-GUESS (v4.1, 97c552c5), *Geosci. Model Dev.*, 18, 4643-4666, 10.5194/gmd-18-4643-2025, 2025.

Olofsson, P., Foody, G. M., Herold, M., Stehman, S. V., Woodcock, C. E., and Wulder, M. A.: Good practices for estimating area and assessing accuracy of land change, *Remote Sens. Environ.*, 148, 42–57, https://doi.org/10.1016/j.rse.2014.02.015, 2014.

O'Sullivan, M., Friedlingstein, P., Sitch, S., Anthoni, P., Arneth, A., Arora, V. K., Bastrikov, V., Delire, C., Goll, D. S., and Jain, A. K.: Process-oriented analysis of dominant sources of uncertainty in the land carbon sink, *Nat. Commun.*, 13, 4781, https://doi.org/10.1038/s41467-022-32416-8, 2022.

Peng, S., Ding, Y., Liu, W., and Li, Z.: 1 km monthly temperature and precipitation dataset for China from 1901 to 2017, *Earth Syst. Sci. Data*, 11, 1931–1946, https://doi.org/10.5194/essd-11-1931-2019, 2019a.

Peng, S., Terrer, C., Smith, B., Ciais, P., Han, Q., Nan, J., Fisher, J. B., Chen, L., Deng, L., and Yu, K.: Carbon restoration potential on global land under water resource constraints, *Nat. Water*, 2, 1071–1081, https://doi.org/10.1038/s44221-024-00295-6, 2024a.

Peng, S., Yu, K., Li, Z., Wen, Z., and Zhang, C.: Integrating potential natural vegetation and habitat suitability into revegetation programmes for sustainable ecosystems under future climate change, *Agric. For. Meteorol.*, 269, 270–284, https://doi.org/10.1016/j.agrformet.2019.02.023, 2019b.

Peng, X., He, G., Wang, G., Yin, R., Yang, R., Peng, Y., Long, T., Zhang, Z., Chen, Y., and Wang, J.: GF-1 WFV satellite images based forest cover mapping in China supported by open land use/cover datasets, *Sci. Data*, 11, 1355, https://doi.org/10.1038/s41597-024-03774-z, 2024b.

Perbet, P., Guindon, L., Côté, J.-F., and Béland, M.: Evaluating deep learning methods applied to Landsat time series subsequences to detect and classify boreal forest disturbances events: the challenge of partial and progressive disturbances, *Remote Sens. Environ.*, 306, 114107, https://doi.org/10.1016/j.rse.2024.114107, 2024.

Piao, S., Fang, J., Ciais, P., Peylin, P., Huang, Y., Sitch, S., and Wang, T.: The carbon balance of terrestrial ecosystems in China, *Nature*, 458, 1009–1013, https://doi.org/10.1038/nature07944, 2009.

Piao, S., Wang, X., Park, T., Chen, C., Lian, X., He, Y., Bjerke, J. W., Chen, A., Ciais, P., and Tømmervik, H.: Characteristics, drivers and feedbacks of global greening, *Nat. Rev. Earth Environ.*, 1, 14–27, https://doi.org/10.1038/s43017-019-0001-x, 2020.

Pugh, T. A. M., Seidl, R., Liu, D., Lindeskog, M., Chini, L. P., and Senf, C.: The anthropogenic imprint on temperate and boreal forest demography and carbon turnover, *Global Ecol. Biogeogr.*, 33, 100–115, https://doi.org/10.1111/geb.13773, 2024.

Qin, Y., Xiao, X., Dong, J., Zhang, G., Shimada, M., Liu, J., Li, C., Kou, W., and Moore III, B.: Forest cover maps of China in 2010 from multiple approaches and data sources: PALSAR, Landsat, MODIS, FRA, and NFI, *ISPRS J. Photogramm. Remote Sens.*, 109, 1–16, https://doi.org/10.1016/j.isprsjprs.2015.08.008, 2015.

Ran, Y., Lu, L., and Li, X.: China Land Cover Classification at 1 km Spatial Resolution Based on a Multi-source Data Fusion Approach, *Adv. Earth Sci.*, 24, 192–203, https://doi.org/10.11867/j.issn.1001-8166.2009.02.0192, 2009.

Ran, Y., Li, X., Lu, L., and Li, Z.: Large-scale land cover mapping with the integration of multi-source information based on the Dempster–Shafer theory, *Int. J. Geogr. Inf. Sci.*, 26, 169–191, https://doi.org/10.1080/13658816.2011.586181, 2012.

Ruehr, S., Keenan, T. F., Williams, C., Zhou, Y., Lu, X., Bastos, A., Canadell, J. G., Prentice, I. C., Sitch, S., and Terrer, C.: Evidence and attribution of the enhanced land carbon sink, *Nat. Rev. Earth Environ.*, 4, 518–534, https://doi.org/10.1038/s43017-023-00456-3, 2023.

Shi, G., Sun, W., Shangguan, W., Wei, Z., Yuan, H., Li, L., Sun, X., Zhang, Y., Liang, H., Li, D., Huang, F., Li, Q., and Dai, Y.: A China dataset of soil properties for land surface modelling (version 2, CSDLv2), *Earth Syst. Sci. Data.*, 17, 517-543, 10.5194/essd-17-517-2025, 2025.

Steidinger, B. S., Crowther, T. W., Liang, J., Van Nuland, M. E., Werner, G. D., Reich, P. B., Nabuurs, G.-J., De-Miguel, S., Zhou, M., and Picard, N.: Climatic controls of decomposition drive the global biogeography of forest-tree symbioses, *Nature*, 569, 404–408, https://doi.org/10.1038/s41586-019-1128-0, 2019.

Sulla-Menashe, D., Gray, J. M., Abercrombie, S. P., and Friedl, M. A.: Hierarchical mapping of annual global land cover 2001 to present: The MODIS Collection 6 Land Cover product, *Remote Sens. Environ.*, 222, 183–194, https://doi.org/10.1016/j.rse.2018.12.013, 2019.

Thonicke, K., Venevsky, S., Sitch, S., and Cramer, W.: The role of fire disturbance for global vegetation dynamics: coupling fire into a Dynamic Global Vegetation Model, *Glob. Ecol. Biogeogr.*, 10, 661–677, https://doi.org/10.1046/j.1466-822x.2001.00175.x, 2001.

Tong, X., Brandt, M., Yue, Y., Horion, S., Wang, K., De Keersmaecker, W., Tian, F., Schurgers, G., Xiao, X., and Luo, Y.: Increased vegetation growth and carbon stock in China karst via ecological engineering, *Nat. Sustain.*, 1, 44–50, https://doi.org/10.1038/s41893-017-0004-x, 2018.

Tu, Y., Wu, S., Chen, B., Weng, Q., Bai, Y., Yang, J., Yu, L., and Xu, B.: A 30 m annual cropland dataset of China from 1986 to 2021, *Earth Syst. Sci. Data*, 16, 2297–2316, https://doi.org/10.5194/essd-16-2297-2024, 2024.

Wei, X., Liu, R., Liu, Y., He, J., Chen, J., Qi, L., Zhou, Y., Qin, Y., Wu, C., and Dong, J.: Forest areas in China are recovering since the 21st century, *Geophys. Res. Lett.*, 51, e2024GL110312, https://doi.org/10.1029/2024GL110312, 2024.

White, J. C., Hermosilla, T., Wulder, M. A., and Coops, N. C.: Mapping, validating, and interpreting spatiotemporal trends in post-disturbance forest recovery, *Remote Sens. Environ.*, 271, 112904, https://doi.org/10.1016/j.rse.2022.112904, 2022.

Winkler, K., Fuchs, R., Rounsevell, M., and Herold, M.: Global land use changes are four times greater than previously estimated, *Nat. Commun.*, 12, 2501, https://doi.org/10.1038/s41467-021-22702-2, 2021.

Xia, X., Xia, J., Chen, X., Fan, L., Liu, S., Qin, Y., Qin, Z., Xiao, X., Xu, W., and Yue, C.: Reconstructing long-term forest cover in China by fusing national forest inventory and 20 land use and land cover data sets, *J. Geophys. Res.-Biogeo.*, 128, e2022JG007101, https://doi.org/10.1029/2022JG007101, 2023.

Xu, H., Yue, C., Zhang, Y., Liu, D., and Piao, S.: Forestation at the right time with the right species can generate persistent carbon benefits in China, *Proc. Natl. Acad. Sci. USA*, 120, e2304988120, https://doi.org/10.1073/pnas.2304988120, 2023.

~~Yang, D., and Song, W.: Tracking land use trajectory to map abandoned farmland in mountainous area, *Environ. Int.*, 75, 102103, https://doi.org/10.1016/j.envint.2022.102103, 2023.~~

Yang, H., Wang, S., Son, R., Lee, H., Benson, V., Zhang, W., Zhang, Y., Zhang, Y., Kattge, J., and Boenisch, G.: Global patterns of tree wood density, *Global Change Biol.*, 30, e17224, https://doi.org/10.1111/gcb.17224, 2024.

Yang, J., and Huang, X.: 30 m annual land cover and its dynamics in China from 1990 to 2019, *Earth Syst. Sci. Data*, 13, 2021–2039, https://doi.org/10.5194/essd-13-2021, 2021.

~~Yang, J. and Huang, X.: 30m annual land cover and its dynamics in China from 1990 to 2019, Zenodo [data], https://doi.org/10.5281/zenodo.4417810, 2021.~~

Yu, Z., Ciais, P., Piao, S., Houghton, R. A., Lu, C., Tian, H., Agathokleous, E., Kattel, G. R., Sitch, S., and Goll, D.: Forest expansion dominates China's land carbon sink since 1980, *Nat. Commun.*, 13, 5374, https://doi.org/10.1038/s41467-022-32909-y, 2022.

Yu, Z., Liu, S., Li, H., Liang, J., Liu, W., Piao, S., Tian, H., Zhou, G., Lu, C., and You, W.: Maximizing carbon sequestration potential in Chinese forests through optimal management, *Nat. Commun.*, 15, 3154, https://doi.org/10.1038/s41467-024-47143-5, 2024.

Yue, C., Xu, M., Ciais, P., Tao, S., Shen, H., Chang, J., Li, W., Deng, L., He, J., and Leng, Y.: Contributions of ecological restoration policies to China's land carbon balance, *Nat. Commun.*, 15, 9708, https://doi.org/10.1038/s41467-024-54019-3, 2024.

Zeng, W., Tomppo, E., Healey, S. P., and Gadow, K. V.: The national forest inventory in China: history-results-international context, *For. Ecosyst.*, 2, 23, https://doi.org/10.1186/s40663-015-0047-1, 2015.

Zhang, M., He, H., Zhang, L., Ren, X., Shi, L., Yu, G., Niu, Z., Qin, K., and Li, T.: Ecosystem engineering and global changes are increasingly enhancing China's terrestrial carbon sinks, *Resour. Conserv. Recycl.*, 223, 108514, https://doi.org/10.1016/j.resconrec.2025.108514, 2025.

Zhu, Y., Xia, X., Canadell, J. G., Piao, S., Lu, X., Mishra, U., Wang, X., Yuan, W., and Qin, Z.: China's carbon sinks from land-use change underestimated, *Nat. Clim. Change*, 15, 428–435, https://doi.org/10.1038/s41558-024-02167-y, 2025.